International Journal of Multiphase Flow 120 (2019) 103105

Contents lists available at ScienceDirect

International Journal of Multiphase Flow

journal homepage: www.elsevier.com/locate/ijmulflow

Inertial particle velocity and distribution in vertical turbulent channel flow: A numerical and experimental comparison

Guiquan Wang[a], Kee Onn Fong[b,c], Filippo Coletti[b,c], Jesse Capecelatro[d], David H. Richter[a,*]

[a] Department of Civil and Environmental Engineering and Earth Sciences, University of Notre Dame, Notre Dame, IN 46556, USA
[b] Department of Aerospace Engineering and Mechanics, University of Minnesota, Minneapolis, MN 55455, USA
[c] St. Anthony Falls Laboratory, University of Minnesota, Minneapolis, MN 55414, USA
[d] Department of Mechanical Engineering, University of Michigan, Ann Arbor, MI 48109, USA

ARTICLE INFO

Article history:
Received 17 April 2019
Revised 9 August 2019
Accepted 3 September 2019
Available online 5 September 2019

Keywords:
Inertial particles
Wall turbulence
Simulations
Experiment

ABSTRACT

This study is concerned with the statistics of vertical turbulent channel flow laden with inertial particles for two different volume concentrations ($\Phi_V = 3 \times 10^{-6}$ and $\Phi_V = 5 \times 10^{-5}$) at a Stokes number of $St^+ = 58.6$ based on viscous units. Two independent direct numerical simulation models utilizing the point-particle approach are compared to recent experimental measurements, where all relevant nondimensional parameters are directly matched. While both numerical models are built on the same general approach, details of the implementations are different, particularly regarding how two-way coupling is represented. At low volume loading, both numerical models are in general agreement with the experimental measurements, with certain exceptions near the walls for the wall-normal particle velocity fluctuations. At high loading, these discrepancies are increased, and it is found that particle clustering is overpredicted in the simulations as compared to the experimental observations. Potential reasons for the discrepancies are discussed. As this study is among the first to perform one-to-one comparisons of particle-laden flow statistics between numerical models and experiments, it suggests that continued efforts are required to reconcile differences between the observed behavior and numerical predictions.

1. Introduction

Over the last several decades, a large number of experimental studies have been dedicated to understanding fluid-particle interactions in turbulent channel flows (Balachandar and Eaton, 2010). In the near-wall region, Kaftori et al. (1995a,b) observed that the behavior of particles is correlated with near-wall coherent structures in the dilute, near-neutral buoyancy limit ($\rho_p/\rho_f = 1.05$, $St^+ = 0.065 - 18$ where St^+ is the particle Stokes number based on wall units). In the core region of the channel, Fessler et al. (1994) found that particles form clusters of length scale O(10 η), where η is the Kolmogorov length scale for moderate inertia particles ($St^+ = 27 - 150$) with mass fractions ranging from $\Phi_m = 0.03 - 1.0$. Kulick et al. (1994) investigated the turbulence modification by high inertia particles ($St^+ = 292 - 2030$) by comparing each over a range of mass loading up to $\Phi_m = 0.8$. Furthermore, Benson et al. (2005) studied the effect of mass loading and wall roughness for high inertia particles ($St^+ = 2630$), which was further numerically investigated by Capecelatro and Desjardins (2015) and Vreman (2015). Recently, Fong et al. (2019) studied in detail the particle spatial distribution both close to the wall and in the centerline of a vertical channel, along with series of particle statistics at relatively low Reynolds numbers and multiple mass fractions. With moderate Stokes number ($St^+ = 64 - 130$), they found a significant difference (particle distribution and particle fluctuation velocity) between mass loading $\Phi_m = 6 \times 10^{-3}$ and $\Phi_m = 0.1$.

Despite the aforementioned experimental progress, measurement of the carrier-phase velocity field near the particles remains a major problem in studying turbulence modulation due to the presence of particles. At the same time, numerical approaches have become a powerful tool to help fill the entire parameter space and understand statistics and mechanisms that are difficult to observe. In turbulent dispersed multiphase flow computations, the most accurate numerical method is the resolved-particle direct numerical simulation (DNS) of finite-size particle-laden turbulent flows, see the review paper of Maxey (2017) and a recent benchmark test of three popular numerical methods for particles by de Motta et al. (2019). However, the resolved-particle DNS is too expensive which limits the number of particles. In order to access a very large ensemble of particles, a popular approach is the

* Corresponding author.
E-mail address: david.richter.26@nd.edu (D.H. Richter).

https://doi.org/10.1016/j.ijmultiphaseflow.2019.103105
0301-9322/

Lagrangian point-particle approach coupled with DNS based on the point-particle approximation, see Squires (2007). The Lagrangian point-particle approach has been able to successfully capture certain phenomena such as particles' preferential accumulation and modulation of turbulence (Poelma and Ooms, 2006; Balachandar and Eaton, 2010), but challenges still persist in achieving quantitative prediction, e.g. improving the point-particle approach by extending its application to finite-size particles (Akiki et al., 2017).

According to the standard paradigm, when Φ_v is small (in the range of $\Phi_v \leq 10^{-6}$), the particles have a negligible effect on the turbulence (i.e. one-way coupling). Here, particles are transported by turbulent motions, and efforts have been aimed at describing this dispersion process. Marchioli and Soldati (2002), for instance, associated particle re-entrainment mechanisms with the strongly coherent ejections and sweeps. Meanwhile, Narayanan et al. (2003) found that particles ($St^+ = 5,\ 15$) preferentially accumulate in the so-called low-speed streaks and tend to deposit on the wall in an open channel flow. In order to compare different numerical predictions, the low order statistics of both particle and carrier phase is benchmarked by Marchioli et al. (2008) for one-way coupled turbulent channel flows.

When Φ_v is moderate (in the regime of $10^{-6} \leq \Phi_v \leq 10^{-3}$), the particles can have a considerable effect on turbulence through momentum exchange (i.e. two-way coupling), especially when particles accumulate in certain regions of the flow. In comparison with one-way coupling, similar particle deposition behaviour has been observed over a wide particle parameter space ($St^+ = 0.055 - 0.889$ in Pan and Banerjee (1995); $St^+ = 1 - 100$ in Sardina et al. (2012); $St^+ = 1 - 100$ in Nilsen et al. (2013); $St^+ = 8.5 - 714$ in Richter and Sullivan (2013) and $St^+ = 4.44 - 444$ in Wang and Richter (2019a)). However, Li et al. (2001) and Nasr et al. (2009) showed that two-way coupling weakened the preferential distribution of particles compared with one-way coupling in the channel flow. In addition to turbulence modulation, low-inertia particles ($St^+ = O(1)$) induce a destabilization effect on transition from laminar to turbulent flow, whereas large-Stokes-number particles ($St^+ > O(10)$) actually stabilize the turbulence Klinkenberg et al. (2011); Wang and Richter (2019a); this is sometimes accompanied by observed drag reduction in numerical models (Li et al., 2001; Dritselis and Vlachos, 2008).

With further increase of particle loading, collision between particles takes place and modifies both particle and fluid statistics (i.e. four-way coupling). The particle/particle collision weakens the preferential distribution of particles (Li et al., 2001; Nasr et al., 2009), and reduces maximum near-wall concentrations (Kuerten and Vreman, 2015). The particle/wall collisions also affect the particle-induced turbulence modulation (Vreman, 2015). In addition, particles at high mass loading tend to decrease the thickness of the boundary layer and increase the skin friction (Vreman et al., 2009), and act as the primary source of turbulence generation (Capecelatro et al., 2016; 2018).

Overall, this broad range of numerical investigations has relied heavily on the use of the point-force approximation, which is widely applied for systems with large numbers of small, heavy particles; see Li et al. (2001); Klinkenberg et al. (2013); Zhao et al. (2013); Gualtieri et al. (2013); Lee and Lee (2015); Vreman (2015); Wang and Richter (2019c); Wang and Richter (2019b). While experimental and numerical efforts have made significant progress in understanding the complex problem of particle-laden turbulent channel flow, there remains a continued lack of comparison and validation between consistent numerical and experimental observations (Eaton, 2009). This is especially for moderate inertia ($St^+ = O(10)$) particles with volume concentrations in the regime of two-way coupling and four-way coupling, since most comparisons have been done for high Stokes number(e.g. Benson et al. (2005)). Under these circumstances, preferential concentration and turbophoresis are at play, particle/particle and particle/wall collision might take place, and particles may modify fluid momentum. In this context, we leverage the recent experimental data of Fong et al. (2019) and perform a statistical comparison between DNS simulations from independent numerical codes (considering both two- and four-way coupling), particularly focusing on particle statistics and clustering behaviour. We aim at investigating (*i*) particle/particle and particle/wall collisions; (*ii*) the difference between the numerical predictions of a traditional point-force method with a more advanced volume-filtering method; and (*iii*) the discrepancies between numerical simulations and experimental results in a Reynolds number, Stokes number, and mass fraction regime which can be achieved using DNS.

2. Simulation method

This study is based on comparing two different numerical models (Richter and Sullivan (2013) and Capecelatro and Desjardins (2013)) to the experiments of Fong et al. (2019). Here we describe the two DNS-based models.

2.1. Point particle method

In this section, the numerical method of Richter and Sullivan (2013) is introduced and compared with existing simulations in the literature, including Zhao et al. (2013), Capecelatro and Desjardins (2015), Vreman (2015), as well as experimental measurements from Kulick et al. (1994), Paris (2001) and Benson et al. (2005). The purpose here is to first compare against existing data before performing our more detailed validation below.

Direct numerical simulations of single-phase flows are performed for an incompressible Newtonian fluid, and this model has been utilized previously in other studies (Richter and Sullivan, 2013; 2014). A pseudospectral method is employed in the periodic directions (streamwise x and spanwise z), and second-order finite differences are used for spatial discretization in wall-normal, y direction. The solution is advanced in time by a third-order Runge–Kutta scheme. Incompressibility is achieved via the solution of a pressure Poisson equation. The fluid velocity and pressure fields are a solution of the continuity and momentum balance equations in Eqs. (1) and (2), respectively:

$$\frac{\partial u_j}{\partial x_j} = 0, \tag{1}$$

$$\frac{\partial u_i}{\partial t} + u_j \frac{\partial u_i}{\partial x_j} = -\frac{1}{\rho_f}\frac{\partial p}{\partial x_i} + \nu \frac{\partial u_i}{\partial x_j \partial x_j} + \frac{1}{\rho_f} F_i + \delta_{i1} g. \tag{2}$$

Here u_i is the fluid velocity, p is the pressure, F_i is the particle feedback force to the carrier phase computed by projecting the particle force to the nearest Eulerian grid points, g is the acceleration of gravity, ν is the fluid kinematic viscosity, and ρ_f is the fluid density.

Particle trajectories and particle-laden flow dynamics are based on the point-force approximation where the particle-to-fluid density ratio $r \equiv \rho_p/\rho_f \gg 1$ and the particle size is smaller than the smallest viscous dissipation scales of the turbulence. As a consequence of this and the low volume concentrations (a maximum bulk volume fraction of $\overline{\Phi_V}$ less than 1×10^{-3}), only the Schiller–Naumann (Schiller, 1933) hydrodynamic drag force is considered. The velocity of particle n is governed by Eq. (3) and particle trajectories are then obtained from numerical integration of the equation of motion in Eq. (4):

$$\frac{du_{p,i}^n}{dt} = f_i^n + f_i^c + \delta_{i1} g, \tag{3}$$

$$\frac{dx_i^n}{dt} = u_{p,i}^n, \tag{4}$$

where the drag is given by

$$f_i^n = \frac{1}{\tau_p}[1 + 0.15(Re_p^n)^{0.687}](u_{f,i}^n - u_{p,i}^n). \tag{5}$$

Here, $\tau_p = \rho_p {d_p}^2/18\mu$ is the Stokes relaxation time of the particle, and the particle Reynolds number $Re_p^n = |u_{f,i}^n - u_{p,i}^n|\, d_p^n/\nu$ is based on the magnitude of the particle slip velocity $(u_{f,i}^n - u_{p,i}^n)$ and particle diameter d_p^n. In this work, the average Re_p^n is less than 1.0, which is far smaller than the suggested maximum $Re_p \approx 800$ for the Stokes drag correction in Eq. (3) (Schiller, 1933). As a result of the low Re_p, the correction to the Stokes drag is minimal in this study. Other terms in the particle momentum equation (see Maxey and Riley, 1983) are neglected since they remain small compared with drag when the density ratio $r \gg 1$. In all simulations, particles are initially distributed at random locations throughout the channel.

In the two-way coupling configuration, particle-particle collisions are not taken into consideration, and we exert a purely elastic collision between particles and the upper/lower walls. This purely elastic wall collision is commonly used in gas-solid turbulence (Li et al., 2001; Sardina et al., 2012; Zhao et al., 2013), however we have tested the restitution coefficient $|u_{p,init}^n/u_{p,final}^n|$ between 0.5 and 1 and do not observe significant changes to particle distributions or two-way coupling, consistent with Li et al. (2001). To demonstrate that our implementation provides results that are consistent with other similar numerical models, we provide a comparison to the two-way coupled simulations of Zhao et al. (2013) in Fig. 1. In this test, gravity is not considered, pressure-driven channel turbulence is simulated at a moderate friction Reynolds number of $Re_\tau = 180$ (based on the friction velocity u_τ), and the particle Stokes number normalized by viscous units is $St^+ = 30$. The particle concentration profile, mean velocity, RMS fluctuation velocity, and Reynolds shear stress are shown in Fig. 1 as a function of wall-normal distance. Here we are essentially confirming that the particle-force method is correctly implemented in the code and that it provides nearly identical results to other similar formulations in the two-way coupled regime.

From the two-way coupling formulation described above, four-way coupling can be included as well, where particle/particle and particle/wall collisions are modeled according to a spring-dashpot system. The collision force f_i^c in Eq. (3) is computed by coupling the DNS code to the open source, DEM-based LIGGGHTS package for discrete element methods, applied initially by Kloss et al. (2012). A Hertz-Mindlin contact model is used in the normal and tangential directions to the vector connecting particle centers. In the present study, we set the parameters in the collision model as follows: Young's modulus (5×10^{-5}), Poisson's ratio (0.45), friction coefficient (0.1) and restitution coefficient (0.9). Further details on the numerical implementation and validation of the collision model can be found in Kloss et al. (2012).

2.2. Volume-averaged particle method

This work also utilizes the model of Capecelatro and Desjardins (2013), whose notable difference with the model of Richter and Sullivan (2013) described above is that volume-averaging is used to apply the two-way coupling forces back to the Eulerian mesh; the model of Richter and Sullivan (2013) uses the traditional particle-in-cell method, projecting only to the nearest nodes.

For the carrier phase, the Navier–Stokes equations are solved on a staggered grid with second-order spatial accuracy for both the convective and viscous terms, and a second-order accurate semi-implicit Crank-Nicolson scheme is implemented for time advancement. The volume-averaged Navier–Stokes equations employed in the model of Capecelatro and Desjardins (2013) are given by

$$\frac{\partial \alpha}{\partial t} + \frac{\partial}{\partial x_i}(\alpha u_i) = 0 \tag{6}$$

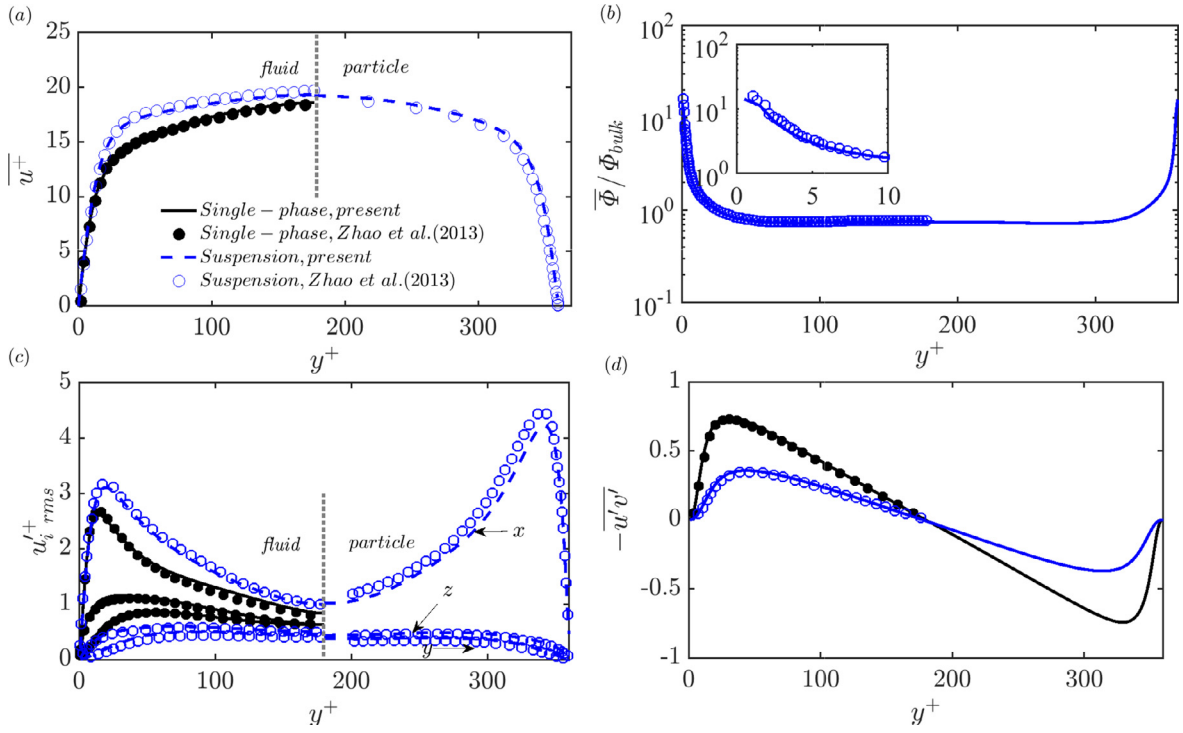

Fig. 1. In comparison with Zhao et al. (2013) pressure-driven channel flow at $Re_\tau = 180$ laden with particles of $St^+ = 30$. (*a*) Mean velocity profile in wall normal direction: left half is the fluid phase and right half is the particle phase; (*b*) Particle concentration profiles in wall-normal direction; (*c*) RMS velocity fluctuation in wall normal direction: left half is the fluid phase and right half is the particle phase; (*d*) Reynolds shear stress of the fluid.

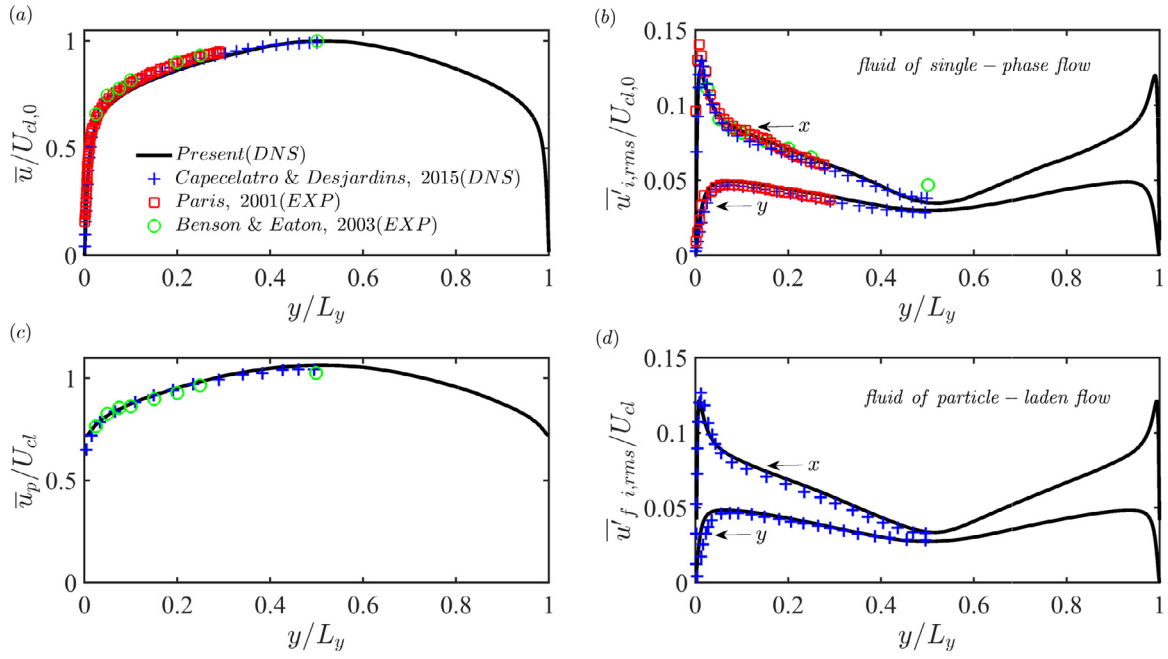

Fig. 2. Comparison with published data at $Re_\tau = 630$ laden with particles of $St^+ = 2030$. (*a*) Mean fluid velocity profile in wall normal direction in single-phase flow; (*b*) fluid RMS velocity fluctuation in wall normal direction in single-phase flow; (*c*) Mean particle velocity profile in wall normal direction; (*d*) RMS fluid velocity fluctuation in wall normal direction in particle-laden flow. All figures are normalized by the fluid centerline velocity.

and

$$\frac{\partial \alpha u_i}{\partial t} + \frac{\partial}{\partial x_i}\left(\alpha u_i u_j\right) = -\frac{1}{\rho_f}\frac{\partial p}{\partial x_i} + \frac{\partial \sigma_{ij}}{\partial x_j} - \frac{\rho_p}{\rho_f}\alpha_p F_i + \alpha \delta_{i1} g, \tag{7}$$

where α is the fluid-phase volume fraction and $\alpha_p = 1 - \alpha$. The fluid-phase viscous-stress tensor is defined as

$$\sigma_{ij} = (\nu + \nu^\star)\left[\frac{\partial u_i}{\partial x_j} + \frac{\partial u_j}{\partial x_i} - \frac{2}{3}\frac{\partial u_k}{\partial x_k}\delta_{ij}\right] \tag{8}$$

where $\nu^\star$ is an effective viscosity that accounts for enhanced dissipation due to unresolved fluid-velocity fluctuations generated at the particle scale (Gibilaro et al., 2007). Unlike in the point-particle description, in this model two-way coupling accounts for both the resolved stresses (pressure and viscous stress) and unresolved fluid stresses (i.e., drag). Thus, the momentum exchange term felt by particle n is

$$f_i^n = \frac{1}{\tau_p}[1 + 0.15(Re_p^n)^{0.687}](u_{f,i}^n - u_{p,i}^n) - \frac{1}{\rho_p}\frac{\partial p^n}{\partial x_i} + \frac{1}{\rho_p}\frac{\partial \sigma_{ij}^n}{\partial x_j}. \tag{9}$$

The momentum exchange term is projected to the grid via

$$\alpha_p F_i = \sum_{n=1}^{N_p} f_i^n \mathcal{G}(|\boldsymbol{x} - \boldsymbol{x}^n|)V_p, \tag{10}$$

where the subscript 'i' refers to the direction of the vector, $V_p = \pi d_p^3/6$ is the particle volume and $\mathcal{G}$ is a Gaussian kernel with characteristic size $\delta_f = 8d_p$. At the walls, a Neumann boundary condition is enforced by introducing an image particle, where the particles close to a wall are mirrored across the boundary. This expression replaces the discontinuous Lagrangian data with an Eulerian field that is a smooth function of the spatial coordinate x_i. Similarly, the fluid volume fraction is computed as

$$\alpha = 1 - \sum_{n=1}^{N_p} \mathcal{G}(|\boldsymbol{x} - \boldsymbol{x}^n|)V_p. \tag{11}$$

To further test the numerical formulations against existing data, we perform a comparison with the simulations of Capecelatro and Desjardins (2015) (focusing only on the dilute regime), which uses the model of Capecelatro and Desjardins (2013). At the same time, we also compare to experimental results from Kulick et al. (1994), Paris (2001), and Benson et al. (2005) under similar conditions, despite the results of Kulick et al. (1994) being subject to unconstrained roughness effects. In this test, turbulent, vertical channel flow is simulated at a high Reynolds number ($Re_\tau = 630$) with high particle Stokes number ($St^+ = 2030$) and a mass loading of $\Phi_m = 0.15$. Fig. 2(a,b) show the mean fluid velocity and RMS fluctuation velocity in single-phase flow; both numerical models agree well with the measurements from Paris (2001) and Benson et al. (2005). In particle-laden flow, the mean particle velocity compares well between numerical models and the measurement from Benson et al. (2005), and the computed RMS fluid fluctuation velocity agrees well between numerical models, as shown in Fig. 2(c,d), respectively.

The particle concentration and particle-phase RMS fluctuation velocity are shown in Fig. 3(a) and (b), respectively. In Fig. 3(a), the concentration profiles between the point particle model and the volume-averaged model of Capecelatro and Desjardins (2015) agree well with each other. In Fig 3(b), Capecelatro and Desjardins (2015) compute a higher RMS particle streamwise velocity compared to the point particle model. In addition, the simulations exhibit a slightly lower RMS wall-normal velocity in the whole channel as compared to the experimental observations of Kulick et al. (1994) and Benson et al. (2005). As a contrast, simulation results from the model of Vreman (2015) are also included in Fig. 3, although the simulations of Vreman (2015) are at a much higher mass fraction ($\Phi_m = 0.7$). The concentration profile is flatter in this case, while the RMS particle velocities are of similar magnitude.

3. Flow and particle parameters

We now turn our attention towards a more detailed validation, which is based on the recent experiments of Fong et al. (2019). The flow configuration of interest is pressure-driven, downwards-oriented channel flow (see Fong et al. (2019)). In the simulations, periodic boundary conditions are applied to both

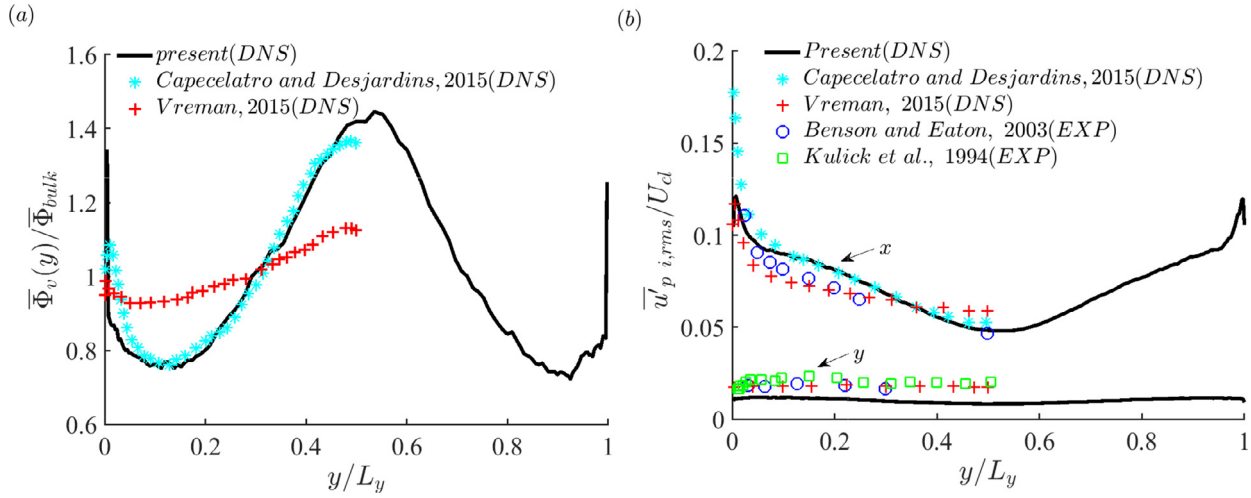

Fig. 3. (*a*) Particle concentration in wall normal direction, the mass loading ($\Phi_v = 7.2 \times 10^{-5}$, $\Phi_m = 0.15$) is same as in present study and Capecelatro and Desjardins (2015), while higher mass loading ($\Phi_v = 9.1 \times 10^{-5}$, $\Phi_m = 0.8$) is used in Vreman (2015); (*b*) RMS particle velocity fluctuation in streamwise direction (x) and wall normal direction (y) normalized by the fluid centerline velocity.

Table 1
Fluid phase parameters for two DNS codes.

	Unladen_R	*Unladen_C*
$h(m)$	15×10^{-3}	
$U_{cl}(m/s)$	4.40	
$U_{bulk}(m/s)$	3.0	
Re_{bulk}	6020	
Re_τ	227	
u_τ	0.227	
δ_v	6.6×10^{-5}	
τ_v	2.9×10^{-4}	
η	$2.0 \times 10^{-4}(centerline)$	
τ_η	$2.6 \times 10^{-3}(centerline)$	
$L_x^+ \times L_y^+ \times L_z^+$	$4276 \times 454 \times 712$	
$N_x \times N_y \times N_z$	$512 \times 128 \times 128$	$656 \times 110 \times 110$
Δx^+, Δz^+	8.35, 5.57	6.52, 6.48

Table 2
Particle parameters. N_p refers to the total number of particles and $V_s \equiv \tau_p g$ refers to the terminal settling velocity in still fluid aligned in the streamwise direction, where g is the gravitational acceleration.

	Low concentration	High concentration
ρ_p/ρ_f	2083	
$d_p(m)$	4.7×10^{-5}	
d_p^+	0.71	
d_p/η	$0.25(centerline)$	
τ_p	0.017	
$V_s(m/s)$	0.167	
St^+	58.6	
St_η	$6.7(centerline)$	
Φ_v	3×10^{-6}	5×10^{-5}
N_p	2.2×10^4	3.67×10^5
Φ_m	6.25×10^{-3}	0.1

phases in the streamwise (x) and spanwise (z) directions. In Fong et al. (2019) two flow Reynolds numbers are used, and we focus on the $Re_{bulk} = 6020$ case, where $Re_{bulk} = 2hU_{bulk}/\nu$ is based on the bulk velocity U_{bulk} and channel height $2h$. This approximately corresponds to $Re_\tau = 227$ based on the friction velocity and h. For the experimental density ratio $\rho_p/\rho_f = 2083$ and diameter $d_p = 4.7 \times 10^{-5}$ m, this corresponds to a Stokes number of $St^+ = 58.6$ based on viscous units and $St_\eta = 6.7$ based on the Kolmogorov scale at the centerline. Two experimental volume loadings are simulated: $\Phi_V = 3 \times 10^{-6}$ ("low") and $\Phi_V = 5 \times 10^{-5}$ ("high").

The fluid-phase flow parameters are provided in Table 1. Throughout, the notation "_R" and "_C" refer to the models of Richter and Sullivan (2013) and Capecelatro and Desjardins (2013), respectively, which were described in Section 2. Both simulations were designed to accurately predict the unladen experiments and match the key nondimensional parameters. The relevant particle parameters are listed in Table 2. The particle diameter is smaller than the Kolmogorov scale η ($d_p/\eta \sim 0.25$), and the conventional understanding is that the point-particle method should yield accurate predictions in this regime.

An overview of the simulations conducted in this study is provided in Table 3. For the model described above, we compare two- and four-way coupling against the experimental data and the four-way coupled model of Capecelatro and Desjardins (2013). A smaller time step is used when four-way coupling is included so that collisions can be resolved. The total simulation time is more than $21h/u_\tau$ and the time for collecting statistics is at least $18h/u_\tau$.

Table 3
Simulations conducted in this study.

	Φ_v	method	Δt^+
Unladen_R	–	–	0.2
low_2_R	low	two-way, point-force	0.2
high_2_R	high	two-way, point-force	0.2
low_4_R	low	four-way, point-force	0.1
high_4_R	high	four-way, point-force	0.1
Unladen_C	–	–	0.13
low_4_C	low	four-way, volume-filtering	0.033
high_4_C	high	four-way, volume-filtering	0.03

4. Preliminary comparisons

4.1. Unladen flow

Comparisons between both numerical models and the measurement produce nearly identical mean velocity profiles, shown in Fig. 4(a,b). In addition, the turbulent intensity profiles and Reynolds shear stress are shown in Fig. 4(c,d), respectively. In the near-wall region, u'_{rms} agrees well whereas v'_{rms}, w'_{rms} and $-\overline{u'v'}$ are slightly higher in *Unladen_R* than for *Unladen_C* and the measurement, which is perhaps due to the different numerical schemes of the flow solvers. In the center region, all components compare well between both numerical models and the experimental observations. The above comparisons indicate that both DNS codes have

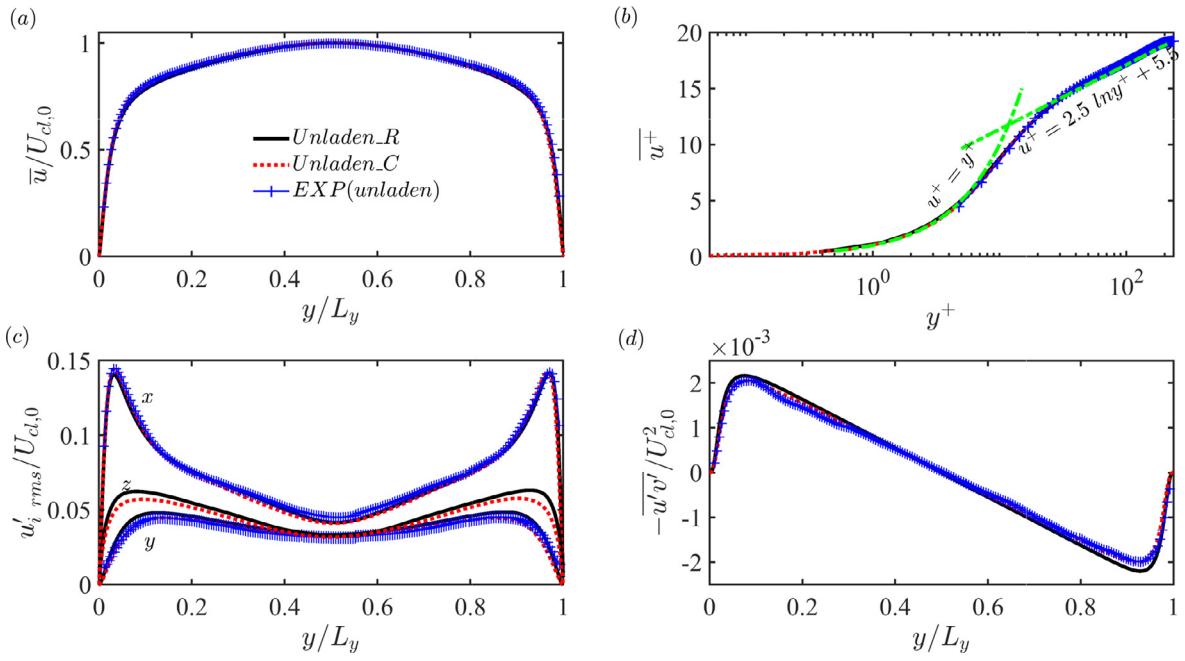

Fig. 4. Unladen velocity statistics comparison between Unladen_R, Unladen_C and the experimental observations of Fong et al. (2019) as a function of wall-normal direction: mean fluid velocity profile in outer units (*a*) and viscous units (*b*); (*c*) RMS fluid velocity fluctuation in three directions; (*d*) Reynolds shear stress. All figures are normalized by the fluid centerline velocity U_{cl}.

successfully captured the large-scale coherent structures in current configuration.

4.2. Time evolution

Before calculating time-averaged statistics, we first investigate the time required to achieve a statistically steady state of the particles as they transition from the uniform initial condition. Two particle timescales are involved: the first is the Stokes timescale τ_p, which indicates how quickly particles can adjust to the local fluid velocity. The second is that associated with mean drift to an equilibrium mean profile, which is typically longer than τ_p. From one-way coupled simulations, Marchioli et al. (2008) found that this time scale is longer for lower inertia particles, e.g., particles with $St^+ = 5$ spend three times as long as particles with a higher $St^+ = 25$ establishing a stationary concentration distribution. The time scale for particles moving to the equilibrium locations influences the length of the development section when performing an experiment. For example Fong et al. (2019) designed the length scale of the development section to be twenty times longer than the particle relaxation time scale multiplied by the centerline fluid velocity with Stokes number of $St^+ = 58.6$.

Fig. 5 shows the time evolution of the domain-averaged RMS particle fluctuation velocity, scaled by the viscous time and velocity scales, respectively. We can see that particle/particle collisions have very little effect on the time to stationarity ($t^+ \sim 400$) at low mass loading, as shown in Fig. 5(a). Comparing Fig. 5(a) and (b), the time required to achieve statistical stationarity at high mass loading is increased by collisions between particles ($t^+ \sim 1200$). For the dimensional values used in the simulations and as a reference for future experiments, these results would suggest that the length of a development section should exceed five times of $\tau_p U_{cl}$ at low mass loading, and twenty times of $\tau_p U_{cl}$ at high mass loading, assuming that particles are randomly distributed initially in a fully-developed turbulent flow field.

To further emphasize this point, the time evolutions of the concentration profiles for cases *high_2_R* and *high_4_R* are shown in Fig. 6(a) and (b), corresponding to the low and high concentrations, and these are compared to experimental measurements. From the simulations, we can see that for both concentrations, particles experience turbophoretic drift, where local maxima are found in concentration near the walls and at the centerline. This drift is enhanced due to the alignment of gravity in the mean flow direction, see for example Capecelatro and Desjardins (2015). The time required to reach a stationary concentration profile is similar to that seen in Fig. 5 for both mass loadings. As compared to the experiments, there is a strong agreement between simulations and observations at low mass loading, except at the wall where simulations overpredict the concentration by nearly a factor of five. At high mass loading, however, the simulations indicate a nearly identical evolution in time and corresponding steady-state concentration profile, while the experiments exhibit a marked change in cross-channel particle distribution at high mass loading. This will be further discussed in Section 5.1.

4.3. Particle accumulation at the walls

As reported by Fong et al. (2019), when standard acrylic walls are used, the concentration profiles start with a strong near-wall peak but drift in time, with particles migrating away from the wall due to collsions with particles adhering to the walls and creating an effective roughness. Due to the roughness, Fong et al. (2019) observed more particles in the center region and fewer particles in the near-wall region, as shown in Fig. 7(a). Based on visual observation, the particle layer which forms with standard acrylic walls covers roughly 10 – 30% of the wall surface. However, after replacing the standard acrylic walls with electrostatic dissipative acrylic walls, particles no longer adhere electrostatically to the wall.

Therefore as an additional test, we artificially place a particle layer at the wall, covering 30% of the wall surface with randomly-located, fixed particles identical in size to the suspension (no two-way coupling feedback is included for these particles). The particle concentration and RMS particle fluctuation velocity are shown in Fig. 7(a) and (b), respectively, for high mass loading. Due to

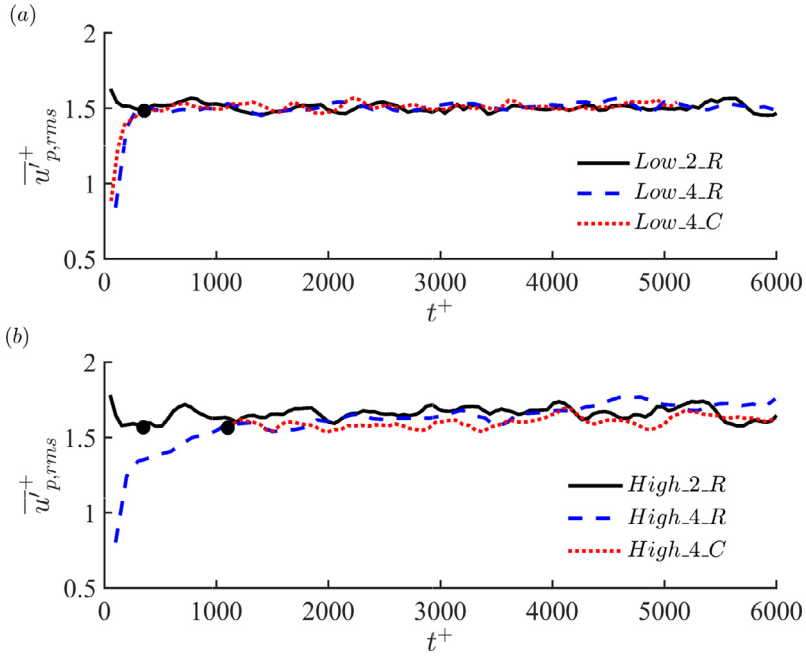

Fig. 5. The domain averaged RMS particle streamwise fluctuation velocity as function of time in (*a*) low concentration and (*b*) high concentration.

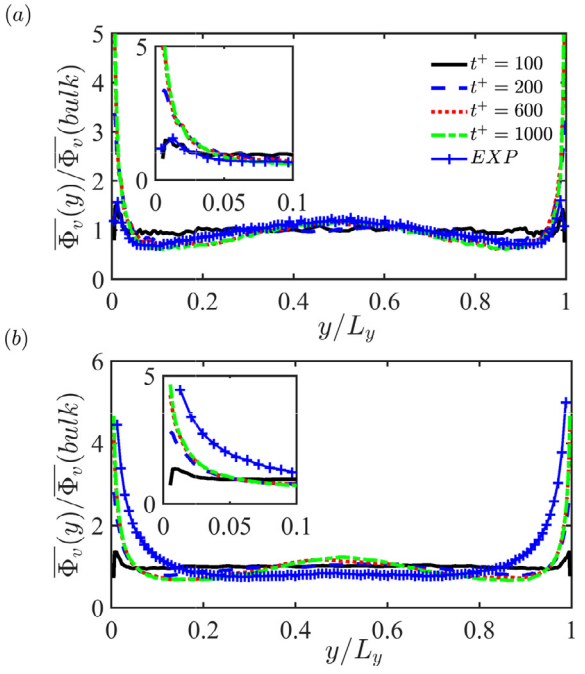

Fig. 6. Particle concentration profiles in wall-normal direction at $t^+ =$ 100, 200, 600, 1000. (*a*) low concentration; (*b*) high concentration. The measurements of Fong et al. (2019) are shown.

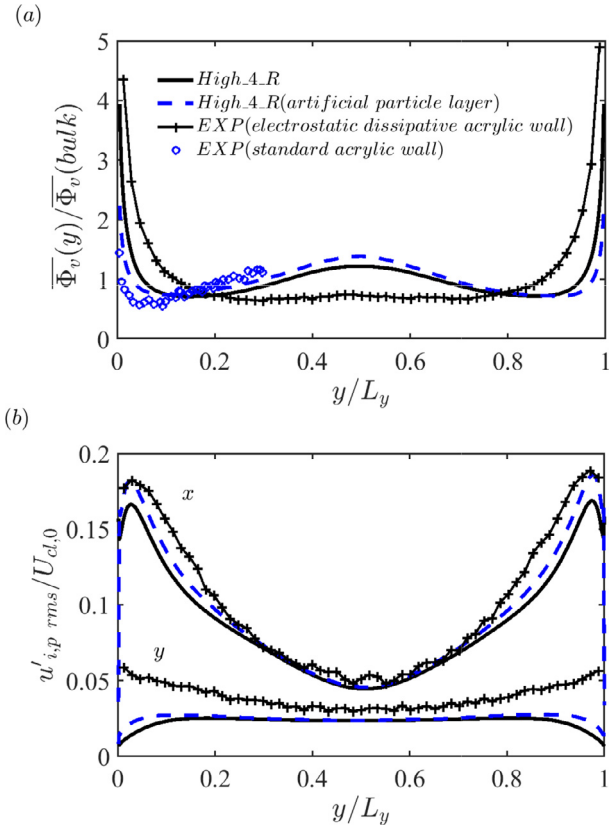

Fig. 7. (*a*) Particle concentration profiles and (*b*) RMS particle fluctuation velocity, as a function of the wall-normal height. Case *high_4_R* with both smooth wall and particle-induced roughness (a particle layer is artificially placed at the wall to represent the roughness) are compared with corresponding experimental observations of Fong et al. (2019).

the presence of this particle-induced roughness, fewer particles are found close to the wall while more particles drift towards the channel center. Particle concentration profiles agree well between the numerical simulation and experimental observations using standard acrylic walls. The increased roughness consequently enhances the RMS particle fluctuation velocity close to the wall, which is consistent with previous investigations of the roughness, e.g., the simulations of (Vreman, 2015) and experiments of Benson et al. (2005). We note that magnitude of these roughness effects is weaker in present study than in previous investigations. This might be due to the fact that the present roughness includes the full particles mounted to the wall, while Vreman (2015) use smaller hemispheres. This results in collisions only between suspended particles with convex surfaces (when hemispheres are mounted on the walls to represent roughness), and this has been seen qualitatively in additional tests (not shown here).

5. Comparison of particle statistics

In this section, the comparison of statistics between the two- and four-way coupled model of Richter and Sullivan (2013), the four-way coupled model of Capecelatro and Desjardins (2013), and the experimental observations of Fong et al. (2019) are shown in detail for both high and low mass loadings. This not only includes the more common statistical quantities including particle concentration profiles, first (i.e. mean velocity) and second order moments (i.e. turbulent kinetic energy and Reynolds shear stress) of the particle phase, but also particle statistics associated with fluid structures (i.e. skewness of the particle and fluid fluctuation velocity, particle concentration dependence of low and high speed streaks), particle clustering behaviours analyzed by domain tessellation techniques (i.e. Voronoï diagram and box counting method), and two-particle statistics (i.e. radial distribution function and angular distribution function). All statistics are taken after a statistically steady state has been achieved (see Fig. 5).

5.1. Particle concentration

The particle concentration profiles normalized by the bulk concentration are shown in Fig. 8. Based on the numerical simulations, low or high mass loading leads to similar particle distributions. With low mass loading as in Fig. 8(a), the profiles nearly overlap between the numerical simulations. In addition, the profile shape is similar between numerical simulations and the experimental measurements, while the influence of turbophoresis in the simulation is stronger at the wall than in the experiment. In both numerical simulations with low mass loading as in Fig. 8(a), the effect four-way coupling is minimal, suggesting that particle-particle collisions are not a dominant effect.

For high mass loading, the particle distribution exhibits a measurable difference when comparing between all numerical simulations with the experimental observations, as shown in Fig. 8(b). From the experiment, the concentration decreases monotonically in the wall-normal direction towards the channel centerline. There

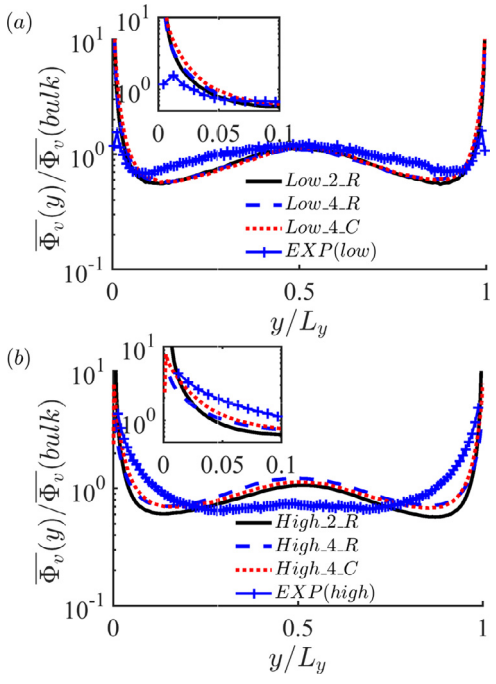

Fig. 8. Particle concentration profile in wall-normal direction, comparison between simulations and the experiment: (*a*) low concentration; (*b*) high concentration.

are more particles in the near-wall region in the case of high mass loading than low mass loading, which corresponds to an opposite trend in the channel center. Above, Fig. 3(a) shows via numerical simulations that very high inertia particles ($St^+ = 2030$) with high mass loading ($\Phi_m = 0.8$) tend to attenuate the turbulence (Vreman, 2015), leading to a flatter concentration profile than with low mass loading ($\Phi_m = 0.15$) (Capecelatro and Desjardins, 2015). Even at these high mass loadings and despite a relatively flattened concentration profile flattened by high mass loading, there still exists a local maxmum in concentration near the channel center. Therefore the discrepancy between the experiments and simulations regarding the sensitivity of $\Phi_V(y)$ to the bulk mass loading remains unclear. But it seems to suggest that at this mass loading the particles are affecting the fluid flow in a way that modifies turbophoresis (Fong et al., 2019). We note that the logarithmic scale of the concentration amplifies these differences.

Inertial particles preferentially accumulate in low-speed streaks — a feature that has been previously observed by both experimental observations (Kaftori et al., 1995a) and numerical investigations (Pan and Banerjee, 1996; Marchioli and Soldati, 2002; Richter and Sullivan, 2013; Wang and Richter, 2019a; 2019c) in different configurations (e.g., channel flow, open channel flow or planar Couette flow) over a wide range of Reynolds numbers ($Re_\tau = 40 - 1000$). In a horizontal open channel flow, Sumer and Deigaard (1981) experimentally found that heavy particles near the bottom are swept into low-speed wall streaks, from whence they are ejected again into the flow. This phenomenon is also observed in current configuration. From the simulation data, we count the particles with $u_p' < 0$ or $u_p' > 0$ to represent particle numbers in low or high speed regions, where u_p' is the particle fluctuation velocity at a particular wall-normal distance. The ratio of $\overline{\Phi_v}(u_p' > 0)$ with $\overline{\Phi_v}(u_p' < 0)$, cast in terms of the effective volume concentration corresponding to these particle counts, is shown in Fig. 9. Simultaneously, Eulerian grid points with $u_f' > 0$ or $u_f' < 0$ are plotted for the unladen flow, where u_f' is the fluid fluctuation velocity. Across the channel, computed results from the numerical simulations agree well with each other. Close to the wall, more particles are in low speed regions than in high speed regions which is opposite compared to the center region. In the near-wall region, this can be explained by the mechanism proposed by Sumer and Deigaard (1981) noted above, that heavy particles near the bottom are swept into low-speed wall streaks, from where they are ejected again into the flow. In the core region of the channel, the preferential sweeping mechanism for a heavy particle interacting with local flow vortical structures under its inertia and the streamwise gravity proposed by Wang and Maxey (1993) is a possible explanation for this.

5.2. Flow and particle velocity statistics

5.2.1. Mean velocity

Mean velocity profiles of the particle phase and carrier phase are shown in Fig. 10, where panels (a,c) are for the low mass loading case and (b,d) are for the high mass loading case. In Fig. 10(a,b), the mean velocity of the particle phase ($\overline{u_p}$) and fluid phase ($\overline{u}$) are shown from numerical simulations, and are normalized by the fluid centerline velocity of the particle-laden flow. Both $\overline{u_p}$ and $\overline{u}$ overlap between the two-way coupling and four-way coupling simulations, indicating that in this dilute limit both two- and four-way coupling have weak impacts on the mean flow. The fluid velocity ($\overline{u}$) lags slightly behind the particle velocity ($\overline{u_p}$) in the majority region of the channel ($0.15 < y/L_y < 0.85$), which is also observed by Capecelatro and Desjardins (2015) and Benson et al. (2005) in vertical channel flow but for a higher

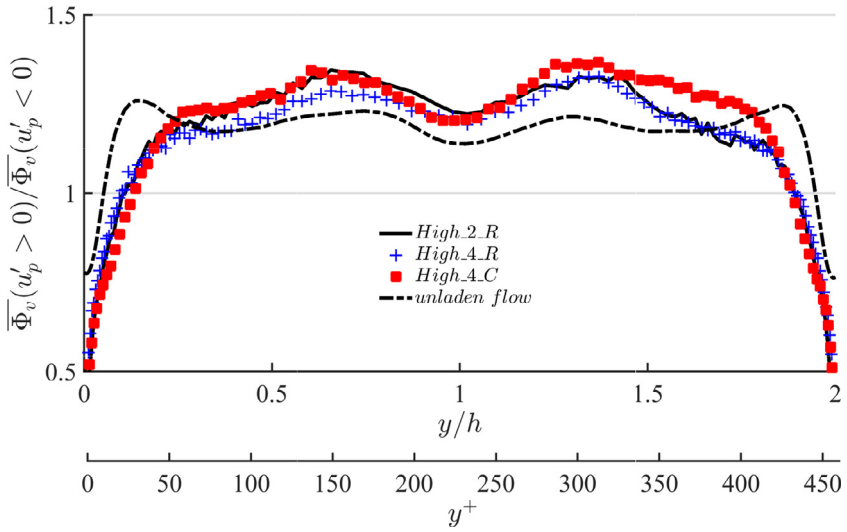

Fig. 9. The ratio between particle concentration with $\overline{\Phi_v}(u_p' > 0)$ and $\overline{\Phi_v}(u_p' < 0)$. For unladen flow, the number ratio of Eulerian grid points with $u_f' > 0$ or $u_f' < 0$ are plotted.

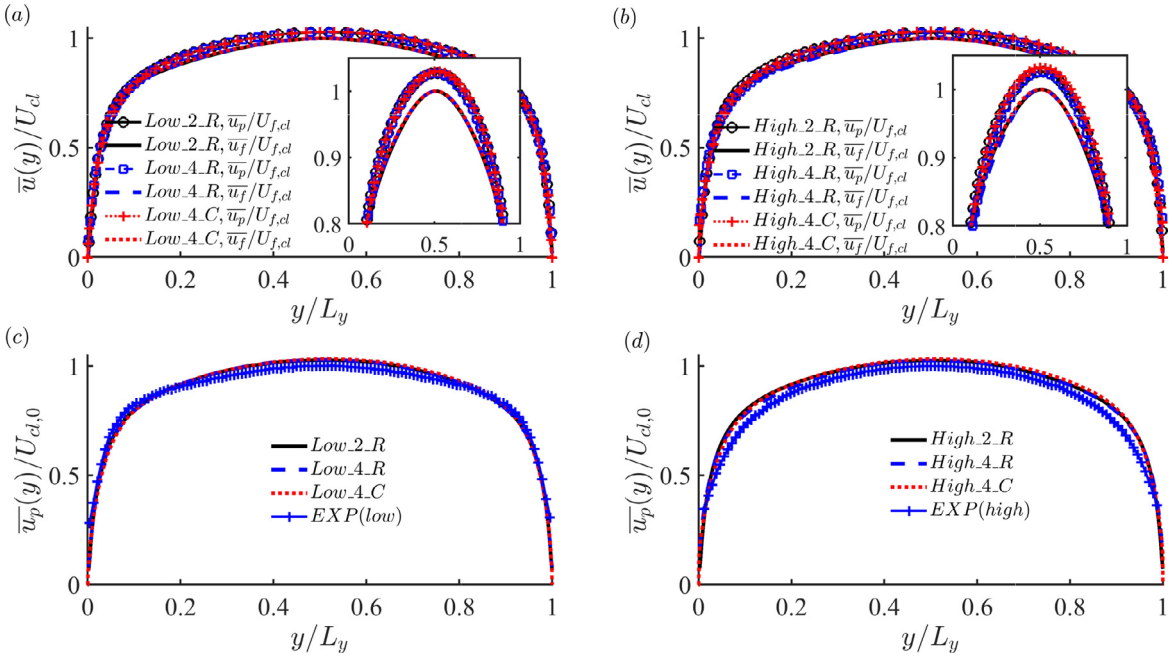

Fig. 10. Mean streamwise velocity in wall-normal direction: (*a, c*) low mass loading; (*b, d*) high mass loading. (*a, b*) Particle phase and carrier phase scaled by the fluid centerline velocity in particle-laden flow; (*c, d*) Particle phase normalized by the fluid centerline velocity in unladen flow.

inertia particles ($St^+ = 2030$). As previously shown in Fig. 9, more particles in high-speed regions away from the wall result in a higher particle average velocity compared to the fluid mean velocity

In Fig. 10(c,d), we compare mean velocity of the particle phase ($\overline{u_p}$) between numerical simulations and experimental observations, normalized by the fluid centerline velocity of unladen flow. Numerical simulations give an almost identical results between low and high mass loading. However, compared with the numerical simulations, the experimentally observed particle average velocity profile is slightly flatter in the case of low mass loading but more parabolic with high mass loading. This higher sensitivity to mass fraction in the experiments as compared to the simulations is similar to that shown in the concentration profiles, but the differences are small ($\Delta\overline{u_p}/\overline{u_p}(EXP) < 5\%$).

5.2.2. Particle velocity fluctuations

Fig. 11 (a,b) and (c,d) show the RMS particle fluctuation velocity in the streamwise and wall-normal directions, respectively. In the streamwise direction, the particle RMS fluctuation velocity is higher than the fluid's close to the wall, especially in the experiment. This is similar to the comparison between the numerical simulations of Capecelatro and Desjardins (2015) with experimental measurements from Benson et al. (2005) for high inertia particles ($St^+ = 2030$). Away from the wall, numerical simulations correspond to the measurements closely. For the wall-normal component of the RMS fluctuation velocity, $v'_{p,rms}$ is smaller than the fluid's across the entire channel, again similar to the experiments of Kulick et al. (1994) for a wide range of Stokes numbers ($St^+ = 400 - 2030$). Close to the wall, the measured profile in Fong et al. (2019) remains fairly flat across the channel and largely

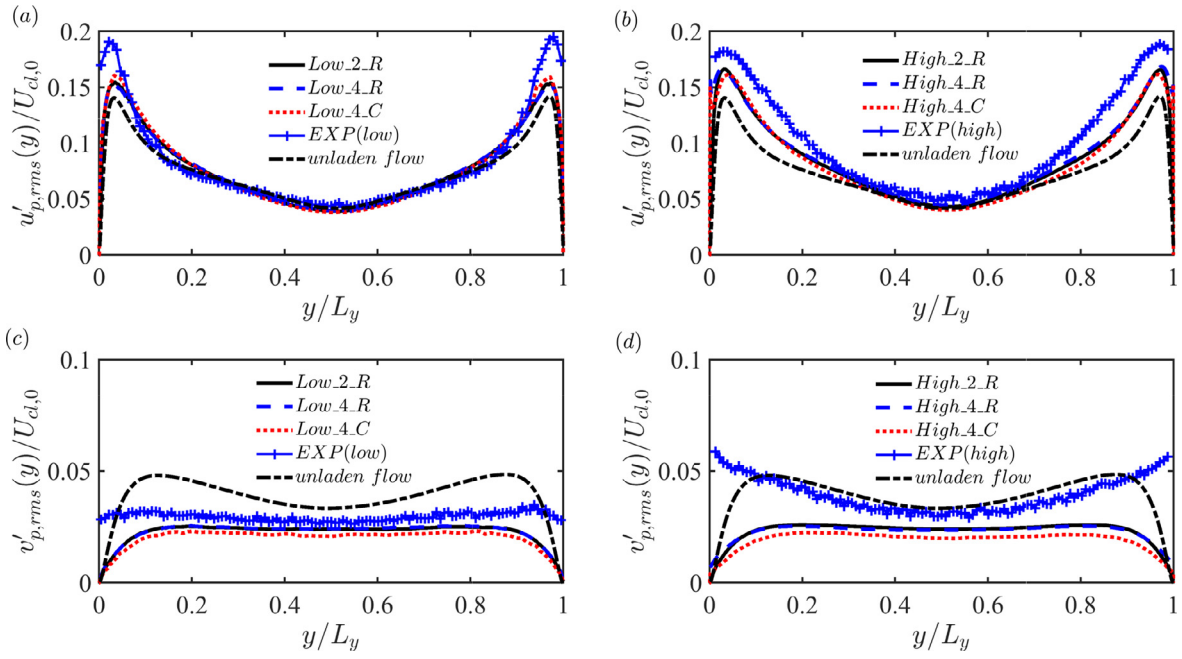

Fig. 11. RMS particle fluctuation velocity in wall-normal direction, normalized by the fluid centerline velocity in unladen flow: (*a, c*) low mass loading; (*b, d*) high mass loading. (*a, b*) RMS particle streamwise fluctuation velocity, $u'_{p,rms}$; (*c, d*) RMS particle wall-normal fluctuation velocity, $v'_{p,rms}$. For comparison, u'_{rms} and v'_{rms} in the simulated case of *Unladen_R* are plotted.

exceeds the unladen fluid levels and it does not appear to vanish. At high mass loading, this difference becomes more enhanced. Again, the simulations exhibit very similar behavior at both mass loadings, while the experiments see an increase in wall-normal particle velocity fluctuations.

The enhanced particle wall-normal fluctuation measured in the experiments consequently contributes to a higher particle Reynolds shear stress as shown in Fig. 12. The discrepancy between numerical simulations with the experiment appears largely confined to the inner layer ($y/L_y < 0.2$ corresponding to $y^+ < 90$) with high mass loading, while they nearly overlap with each other in the channel center (i.e. outer layer $y^+ > 100$).

The computed skewness factor $S(u')$ of the fluctuating velocity distribution (u'_p for the particle and u' for the carrier phase in Eulerian grid) and $S(u'v')$ ($u'_pv'_p$ for the particle and $u'v'$ for the carrier phase) is shown in Fig. 13. Here, negative skewness indicates a heavy tail occurring on the left side of the distribution, and positive skewness indicates that a heavy tail occurs on the right. The skewness factor in Fig. 13(a) for u'_p and u' is also compared with previous DNS data for single-phase flow at $Re_\tau = 180$ computed by Kim et al. (1987). For the carrier phase (u'), there is general agreement between all simulation results (current simulations and Kim et al. (1987)) and measured data, showing a positive skewness factor close to the wall but negative away from the wall, with a crossover point at $y^+ = 20 \sim 30$. In the current numerical simulations, the behaviour of the skewness of u'_p is similar, and the crossover point moves to a higher $y^+ = 50 \sim 65$ compared that for u'. This is consistent with the discussion of Fig. 9, that particles reside more in the low-speed streaks close to the wall but in high-speed streaks away from the wall. Compared to the measured values of $S(u'_p)$, however, a different behavior is seen. The symbols in Fig. 13(a) indicate that the probability distribution of u'_p has a similar shape across the channel, and therefore the skewness of u'_p has an opposite sign with u' away from the wall. This is in contrast to the simulations, which show a similar qualitative behavior between $S(u')$ and $S(u'_p)$.

The skewness of Reynolds shear stress $u'v'$ is shown in Fig. 13(b), which is antisymmetric about the center plane. From the wall to channel center, a negative skewness factor indicates that the tail is always on the left side of the probability distribution of $u'v'$. In single-phase flow, the main contribution of the Reynolds

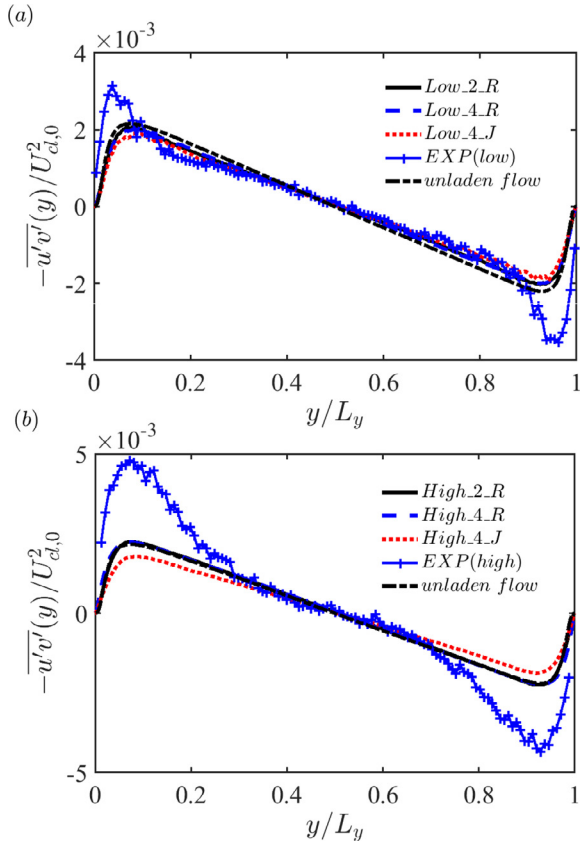

Fig. 12. Particle Reynolds shear stress as a function of wall-normal direction normalized by the fluid centerline velocity in unladen flow: (*a*) low mass loading; (*b*) high mass loading. For comparison, $u'v'$ in the case of Unladen_R is plotted.

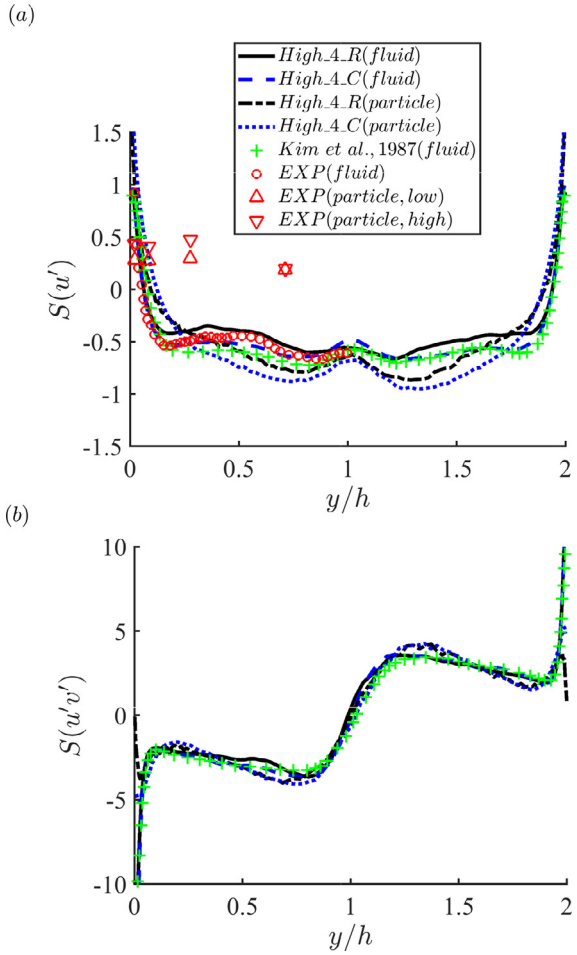

Fig. 13. Skewness factor of both particle and fluid phases in the case of high mass loading: (*a*) $S(u')$ and (*b*) $S(u'v')$. As a comparison, $S(u')$ and $S(u'v')$ of the single-phase flow from Kim et al. (1987) at $Re_\tau = 180$ are plotted.

shear stress is from ejections and sweeps in wall-bounded turbulence (Kim et al., 1987). Consequently, the majority of particle Reynolds shear stress is due to particles in the same ejections and sweeps. In the experiment of Fong et al. (2019), it is not possible to check whether u'_p and u'_f or v'_p and v'_f have the same sign at the particle positions due to the lack of simultaneous carrier phase measurements. However they observed that the majority of the particle Reynolds shear stress is due to the contribution from the second and fourth quadrants of the (u'_p, v'_p) plane.

5.3. Domain tessellation

Particle preferential accumulation is a key feature of inertial particle behavior and has been shown to have a significant impact on turbulence modification (Eaton and Fessler, 1994). When combined with gravitational settling, inertia has been seen to influence the effective settling rate, where particles can fall at speeds not equal to their terminal velocity (Petersen et al., 2019; Wang and Maxey, 1993); this effect is tightly linked to preferential accumulation. Therefore, in this section we show particle clustering behaviours in the current study, and compare them to the results of Fong et al. (2019). There are several techniques to identify clusters of particles, and almost all the methods try to quantify the deviation from a uniform distribution of particles (Monchaux et al., 2012). Following Fong et al. (2019), we focus on Voronoï tessellation and the box counting method in this section.

5.3.1. Voronoï tessellation

Fig. 14 shows instantaneous particle locations and the associated Voronoï diagram in a slab with thickness of $2d_p$ close to the wall ($y/L_y = 0.1$) and in the center region ($y/L_y = 0.5$) of case *high_4_R*. Based on the particle concentration profiles shown in Fig. 8, there are less particles in the former ($y/L_y = 0.1$) than in the latter ($y/L_y = 0.5$), which can be observed in the particle distributions in Fig. 14(a) and (b).

In order to quantify the particle clustering behaviour, we employ a Voronoï diagram analysis, which compares the distribution of the tessellation areas in the particle-laden cases with the expected random Poisson process (RPP) if the particles were uniformly distributed (see for example Monchaux et al. (2012)). Fig. 15 shows the standard deviation ($\sigma_\mathcal{V}$) of the distribution of the normalized Voronoï area $\mathcal{V} = A/\overline{A}$, where the inverse of the average Voronoï area $\overline{A}$ indicates the mean particle concentration. $\sigma_\mathcal{V}$ is scaled by the standard deviation of a random Poisson process (RPP; $\sigma_{RPP} = 0.52$). A ratio $\sigma_\mathcal{V}/\sigma_{RPP}$ exceeding unity indicates that particles are accumulating in clusters as compared to truly randomly distributed particles.

Fig. 15 shows the ratio $\sigma_\mathcal{V}/\sigma_{RPP}$ for multiple wall-normal distances. Across the entire channel, computed results from the two-way coupling configuration is slightly lower than those from both of four-way coupling methods, which indicates that particle clustering is higher when collision forces are included. This is in contrast with previous studies without gravity by Li et al. (2001) and Nasr et al. (2009), who found that particle/particle collisions weakened the preferential distribution of particles. Comparing the two four-way coupling cases, the standard deviation is higher for case *high_4_C* than for *high_4_R* near the wall; aside from this, they have a good agreement with each other away from the wall ($y/h > 0.11$ or $y^+ > 40$). In addition, the ratio $\sigma_\mathcal{V}/\sigma_{RPP}$ increases monotonically with increasing wall-normal distance (towards the center), which indicates that the particle clustering effect is stronger in the center region but weaker in the near-wall region. The measured $\sigma_\mathcal{V}/\sigma_{RPP}$ of Fong et al. (2019) is from particles in slabs with thickness of 17 viscous units. We can see that the measured $\sigma_\mathcal{V}/\sigma_{RPP}$ is lower close to the wall whereas higher in the center compared to the numerical simulations.

5.3.2. Box counting method

The Voronoï diagram analysis compares the distribution of the tessellation areas of the particles with the randomly distributed particles. Besides the Voronoï diagram analysis, here we use the box counting method to compare the particle number in a square box with that for randomly distributed particles; this process explores the length scale on which particle clustering occurs. Thus the deviation of particle number density should be the same for randomly distributed particles when very small or large boxes are used to count for particle number density; see Fessler et al. (1994) and Monchaux et al. (2012).

The box size should be determined in order to capture the maximum deviation from the uniform particle distribution, which can be expressed as $(\sigma_{box} - \sigma_{box,RPP})$ scaled by the mean particle number density. The difference of $(\sigma_{box} - \sigma_{box,RPP})$ is shown in Fig. 16(a) and (b), which is computed in the near-wall region ($y/L_y = 0.12$) and in the channel center ($y/L_y = 0.5$), respectively. Generally, the deviation is larger in the center than that close to the wall, similar to the deviation of the Voronoï diagram analysis in Fig. 15. Specifically, in the near-wall region as in Fig. 16(a), the computed deviation with the use of the two-way coupling method is smaller than the four-way coupling configurations; again this has the same trend as from the Voronoï diagram analysis shown in Fig. 15. In both the near-wall and center regions (Fig. 16(a) and (b), respectively), numerical simulations have similar deviations, however, the magnitudes are higher than the measurements

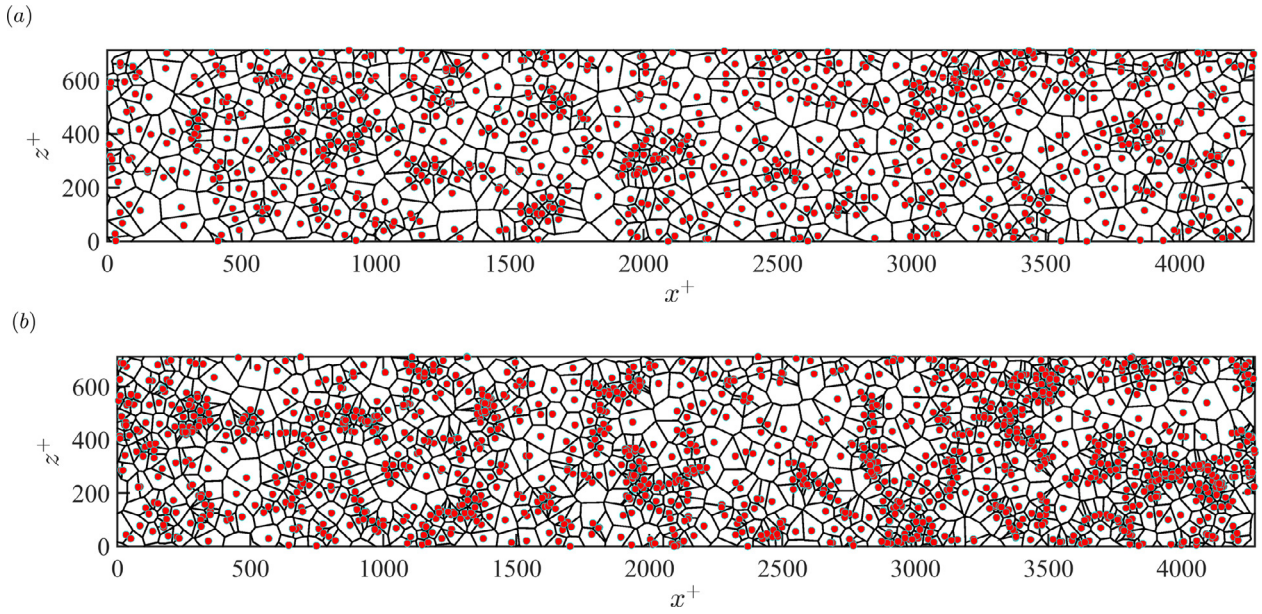

Fig. 14. Particle locations and the associated Voronoï diagram in a wall-normal slab with thickness of $2d_p$ at two wall-normal locations: (a) near-wall region $y/L_y = 0.1$ ($y^+ = 46$); (b) channel center $y/L_y = 0.5$ ($y^+ = 227$).

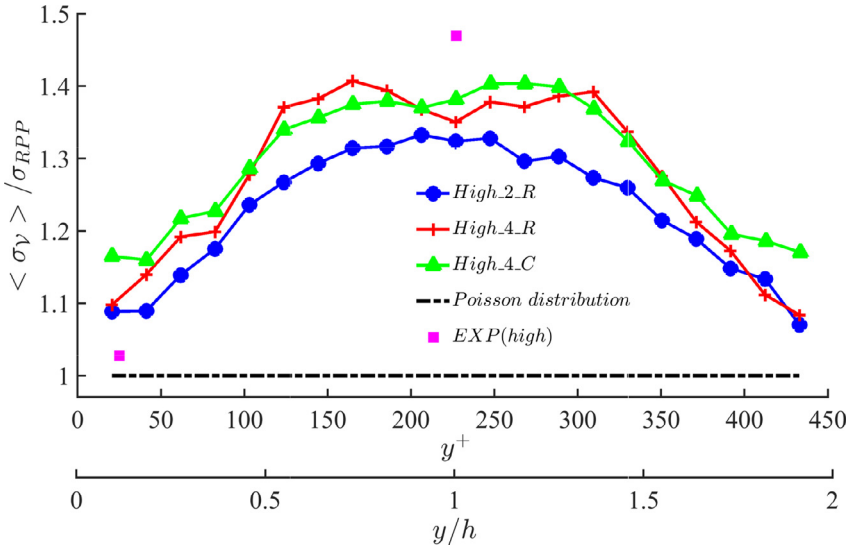

Fig. 15. Standard deviation of the normalized Voronoï area σ_Y in a wall-normal slab with thickness of $2d_p$, normalized by that of a random Poisson process, σ_{RPP} as a function of height in wall-normal direction of the case with high mass loading. Experimental observation from Fong et al. (2019) is shown as a black square close to the wall ($y^+ = 25$) and at the channel centerline.

of Fong et al. (2019). Additionally, the maximum deviation occurs on box length scales of roughly 60 wall units, which is similar to the experimental result from Fessler et al. (1994).

Consequently, particle number density distributions calculated by a box size of 60 wall units ($0.133L_y$) are shown in Fig. 16(c) and (d) for the near-wall region ($y/L_y = 0.12$) and in the channel center ($y/L_y = 0.5$), respectively. The distributions computed by numerical simulations agree well with each other. In the near wall region as shown in Fig. 16(c), the distributions of moderate inertia particles ($St^+ = 58.6$) are different from the randomly distributed particles, even though the deviation of the Voronoï diagram analysis in Fig. 15 is as low as $1.1 \sim 1.2$. The measurements of Fong et al. (2019) show more particles in the box (mean value of 20) than the numerical simulations (mean value of 11), which corresponds to the higher concentration profile in the experiment than in the numerical simulations in the near-wall region (as shown in Fig. 8(b)). The experiment results actually exhibit a near-Poisson distribution which indicates a more uniformly distributed particle layer close to the wall than that from the numerical simulations. In the center region shown in Fig. 16(d), the measured particle number density distribution by Fong et al. (2019) is similar to the current numerical simulations, while there are less particle numbers in the box (mean value of 9.3) than in the numerical simulations (mean value of 19), which corresponds to the lower concentration profile in the experiment than in the numerical simulations in the near-wall region (as shown in Fig. 8(b)). Both the numerical and experimental results show a different distribution from randomly distributed particles, indicating a measurable particle clustering effect in the channel center.

5.4. Two-point statistics: Radial and angular distribution function

The Voronoï diagram analysis and box counting method provide a global metric of clustering without consideration of the cluster anisotropy that frequently appears in the near-wall region. In this regard, another widely used tool to quantify particle

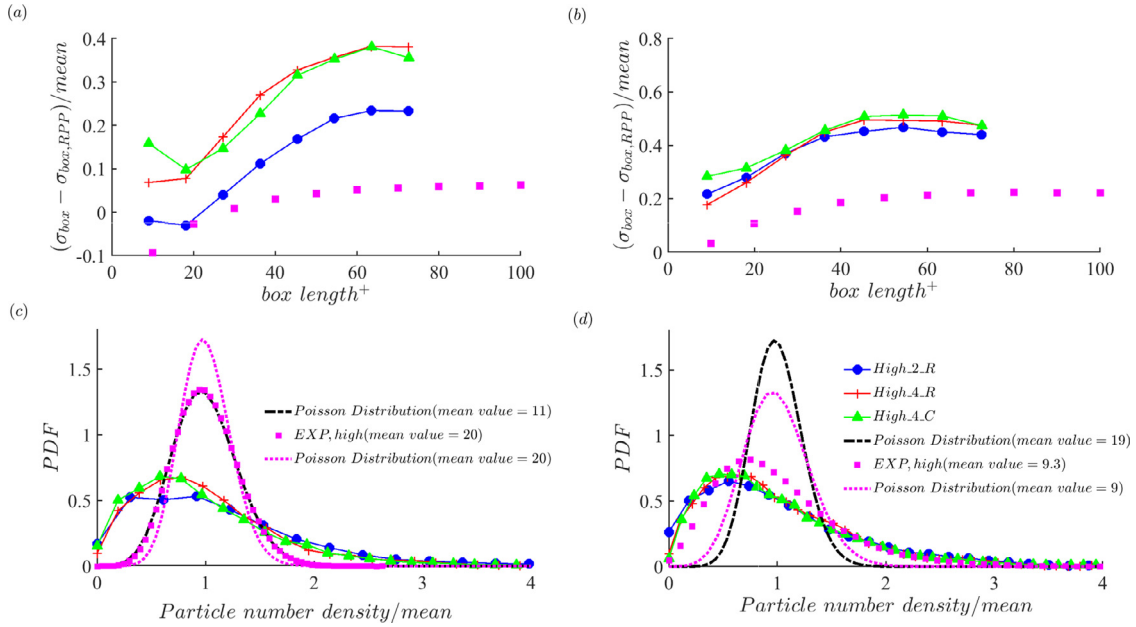

Fig. 16. (a,b) Deviation of particle number density distributions from uniformly distributed particles in a slab, as a function of the length of a square box. (c,d) distributions of particle number density within the slab. Slabs ($\Delta x^+ = 60$ and $\Delta z^+ = 60$) with the thickness of $\Delta y/L_y = 0.036$ ($\Delta y^+ = 17$) are taken at two different wall-normal heights: (a,c) $y/L_y = 0.12$ ($y^+ = 55$); (b,d) $y/L_y = 0.5$ ($y^+ = 227$). Mean value represents for particle number per box.

clustering is the radial distribution function (RDF). The radial distribution function describes how density varies as a function of distance from a reference particle, which has been successfully applied in homogeneous turbulence to determine particle clusters and collision mechanisms, see for example Sundaram and Collins (1997), Barkley and Tuckerman (2007), Gualtieri et al. (2009), and Bragg et al. (2015). However, the RDF still provides only an omni-directional average of particle information (Baker et al., 2017). Thus, an expansion of RDF from 1D to 2D polar coordinates, providing an angular distribution function (ADF), illustrates the anisotropy of particle clustering behaviour in both distance and direction (Gualtieri et al., 2009; Fong et al., 2019).

The two-dimensional radial and angular distribution functions are defined as in Eqs. (12) and (13), where in the simulations particles are taken from a slab with thickness of $0.036L_y$ (17 viscous units):

$$RDF(r) = \frac{\sum_{i=1}^{n_p} \delta N_i(r)/(\delta r \cdot n_p)}{N/(L_x \cdot L_y)}, \tag{12}$$

$$ADF(r,\theta) = \frac{\sum_{i=1}^{n_p} \delta N_i(r,\theta)/(\delta r \cdot \delta\theta \cdot n_p)}{N/(L_x \cdot L_y)}, 0 \le \theta \le \pi/2, \tag{13}$$

where $\delta N_i(r)$ is the particle number between $r - \delta r/2$ and $r + \delta r/2$ from the center of particle i, and $\delta N_i(r, \theta)$ is the particle number in a sector between $r - \delta r/2$ and $r + \delta r/2$ in the radial direction and $\theta - \delta\theta/2$ and $\theta + \delta\theta/2$ in the angular direction from the center of particle i; $\theta = 0$ and $\theta = \pi/2$ correspond to the spanwise and streamwise directions, respectively. In the present study, we set $\delta r = 0.05h$ ($\delta r^+ = 11.4$) and $\delta\theta = 0.025\pi$ to compute $RDF(r)$ and $ADF(r, \theta)$. The mean value is from the average of n_p particles from multiple snapshots in time. Finally, the distribution functions are normalized by the surface average particle number in $x - z$ plane (n_p/L_xL_y representing a randomly distributed particle number density), where n_p particles are from a two-dimensional $x - z$ slab taken in the wall-normal direction. Periodic boundary conditions are used for particles near the boundaries in the streamwise and spanwise directions.

Close to the wall, particle preferential accumulation in streaky structures has been observed both numerically (e.g. Rouson and Eaton (2001)) and experimentally (e.g. Kaftori et al. (1995a)). The clustering of particles preferably appears for moderate Stokes number particles, i.e. $St^+ = O(10)$ (Wang and Richter, 2019a). The RDF and ADF of particles in a slab close to the wall ($y = 0.11h - 8.5\delta_v$ to $y = 0.11h + 8.5\delta_v$) for the case of high mass loading is shown in Fig. 17. Comparing between Fig. 17(a) and (c), the computed RDF based on four-way coupling point-force method is weaker than that based on the volume-filtering method. The streamwise RDF decreases to unity (unity indicates a random distribution) at $r/h > 2$ ($r^+ > 454$) whereas the spanwise RDF decreases to unity at $r/h \sim 0.2$ ($r^+ \sim 46$), which indicates that the anisotropic content of particle cluster is stronger in the streamwise direction than in the spanwise direction.

Meanwhile, we also calculate the RDF of particles in a slab with thickness of $\Delta y^+ = 8$ and 30 compared with $\Delta y^+ = 17$. We find that the thickness of the slab only has a slight effect on the spanwise and global RDFs (figure not shown). However as shown in Fig. 17(a) and (c), the streamwise RDF decreases with increasing thickness of the slab. The computed RDF is noticeably more correlated than the measured RDF in Fong et al. (2019), especially near the wall, consistent with the box-counting analysis shown previously.

Furthermore, Fig. 17(b) and (d) depict the two-dimensional correlation of particle pairs in both spanmwise and streamwise directions, based on cases *high_4_R* and *high_4_C*, respectively. Clearly, the computed ADF by case *high_4_C* is more correlated than case *high_4_R*, in both the streamwise and spanwise directions (the streamwise and spanwise ADF is the same as the streamwise and spanwise RDF as shown in Fig. 17(a) and (c), respectively). The distance from the maximum ADF to minimum ADF in the spanwise direction is around $\Delta r = 0.4h$ ($\Delta r^+ = 91$), which is comparable to the well-known streak spacing ($\Delta z^+ \sim O(100)$) between low with high speed streaks in single-phase flow. Additionally, this strong spanwise correlation is consistent at wide angles, due to the well-organized alternating low and high speed streaks.

Away from the wall, in the central region of the channel, the turbulence tends to be more isotropic. Fig. 18 shows RDF and ADF of particles in a slab along center plane ($y = h - 0.015h$ to $y = h + 0.015h$) for the case with high mass loading. Similar to the

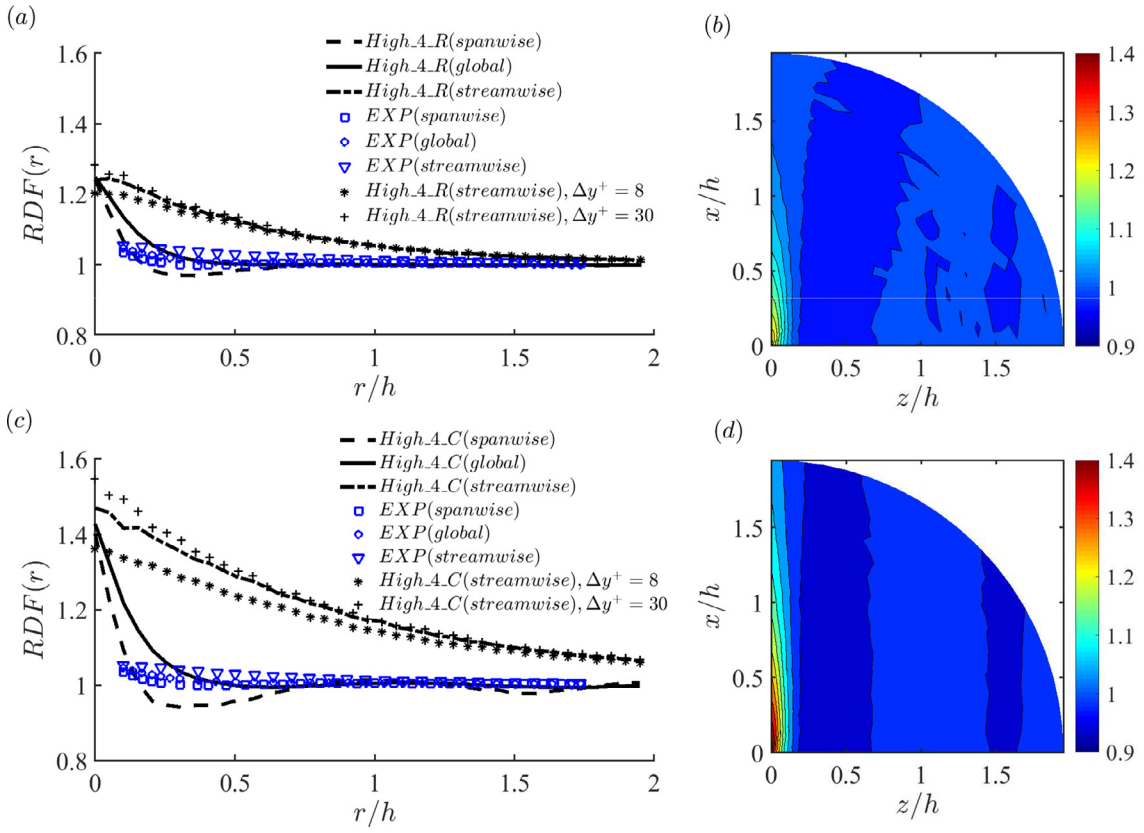

Fig. 17. RDF and ADF of particles in a slab with thickness of $\Delta y^+ = 17$ close to the wall ($y = 0.11h - 8.5\delta_v$ to $y = 0.11h + 8.5\delta_v$) in the case of high mass loading: (a,c) Global RDF, streamwise RDF (equals to $ADF(r, \theta = \pi/2)$) and spanwise RDF (equals to $ADF(r, \theta = 0)$). Streamwise RDF in a slab with thickness of $\Delta y^+ = 8$ and 30 is shown as a comparison, where spanwise and global RDF is similar between $\Delta y^+ = 17$ with $\Delta y^+ = 8$ and 30; (b,d) Contours of ADF in the $x - z$ plane. (a,b) Case *high_4_R*; (c,d) Case *high_4_C*.

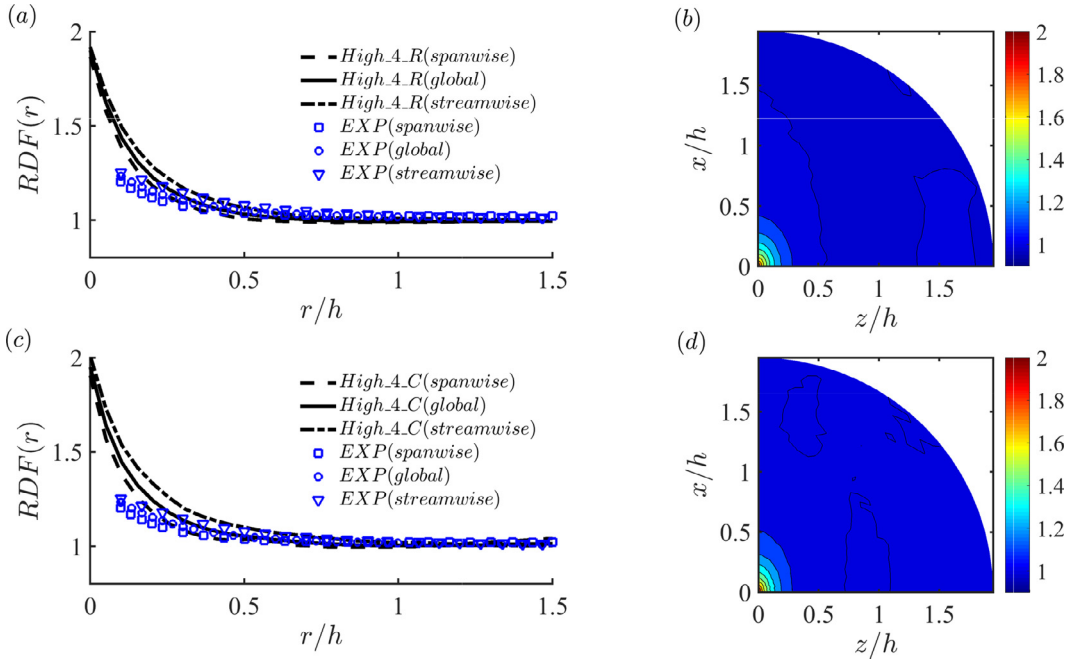

Fig. 18. RDF and ADF of particles in a slab with thickness of $\Delta y^+ = 17$ along the center plane ($y = h - 8.5\delta_v$ to $y = h + 8.5\delta_v$) in the case of high mass loading: (a,c) Global RDF, streamwise RDF (equals to $ADF(r, \theta = \pi/2)$) and spanwise RDF (equals to $ADF(r, \theta = 0)$); (b,d) Contours of ADF in the $x - z$ plane. (a,b) Case *high_4_R*; (c,d) Case *high_4_C*.

near-wall particle RDFs, the simulated RDFs are clearly more correlated than the experimental RDFs of Fong et al. (2019) whereas the simulated RDFs based on both four-way coupling methods agree with each other. From the contours of the ADFs in Fig. 18(b,d), there is significantly less anisotropy of particle clustering in the channel center than in the near-wall region.

6. Conclusion

In this study, we investigate a vertical turbulent channel flow laden with moderate inertia particles ($St^+ = 58.6$) in the regime of two-way coupling to four-way coupling, with gravity aligned in the streamwise direction. Computed results from two independent DNS codes (based on point-force and volume-filtering methods), are compared directly with experimental measurement.

Initially, particles are distributed randomly across the turbulent channel and gradually achieve a steady state, characterized by the particle turbophoresis time scale. Based on numerical simulations, particle/particle and particle/wall collisions have a negligible effect on the particle development time scale at low mass loading ($\Phi_m = 6 \times 10^{-3}$), while collisions tend to delay the particle development time scale at high mass loading ($\Phi_m = 0.1$). When there is a fixed particle layer attached to each wall, more particles drift towards the center region from the near wall region, and the computed particle concentration profile was similar to measurements obtained using walls on which particle depositions had occurred.

For low mass loading ($\Phi_m = 6 \times 10^{-3}$), the two-way coupling approach and both four-way coupling codes give nearly the same statistical profiles (e.g., particle mean velocity profile, concentration profile, particle RMS fluctuation velocity, particle Reynolds shear stress, and particle velocity skewness). On the other hand, there are more particles near the wall in simulations than observed in the experiment, which indicates that turbophoresis is stronger in the computational models than in the experiment. A plausible explanation for this is the missing lift force in the pointwise particle method (Marchioli et al., 2007), which is due to the combination of short-range particle-wall interactions and local shear rate; see the recent work of Costa et al. (2019) who show that turbophoresis is stronger in the pointwise particle method than it is in interface-resolved method. In spite of this discrepancy, computed results agree well with the measurement away from the wall. However, with increased mass loading to $\Phi_m = 0.1$, more particles drift towards the channel center, and the experimental measurement suggests a dramatic turbulence modification with mass loading which is not observed in numerical simulations (even laden with greater number of higher inertia particles).

Particle clustering behaviours are analysed by Voronoï diagram analysis, box counting, and radial distribution functions in the case of high mass loading. Particle preferential concentration is strengthened with use of four-way coupling. This result is opposite to that of previous investigations in Li et al. (2001) and Nasr et al. (2009), who do not consider streamwise gravitational settling. Additionally, the angular distribution function is calculated in order to gain insight into the anisotropy of particle clusters. In the near-wall region, particle preferential concentration is higher in the streamwise direction than in the spanwise direction, especially in numerical simulations. Furthermore, the correlation coefficient is higher with the use of the four-way coupling volume-filtering method than point-force method. In the near-wall region, the mean distance of particle pairs correlates to the well-known streak spacing between the alternating low and high speed streaks in the single-phase flow. However, in the center region, both the particle clusters and turbulence structures tend to be more isotropic than in the near-wall region seen in both experiments and numerical simulations.

Taken together, these observations point to unmet challenges in modeling the behavior of wall-bounded particle-laden flows as measured in the laboratory. The uncertainties associated to the experiments should not be underestimated: the test case in Fong et al. (2019) was designed to remove some of the confounding factors present in previous studies, specifically the static charge on the walls that leads to particle adhesion and unwanted roughness. However, it is possible that unquantified triboelectric effects were still present, affecting particle-wall and particle-particle interactions. The incomplete streamwise development and residual turbophoretic drift may also have impacted the statistics. The finite channel aspect ratio (8:1) would not be considered a major factor in a single-phase flow, but the exact impact on the particle-laden case has not been addressed. In general, even in a relatively simple setting, to exactly identify all the consequential factors and all the important physical processes remains a challenge.

On the other hand, point-particle DNS has well known limitations in accounting for two-way coupling between particles and fluid flows, which motivated a number of recent efforts (Horwitz and Mani, 2016; Ireland and Desjardins, 2017). However, at the considered concentrations and particle Reynolds numbers, it is not obvious how the classical mechanisms by which particles would affect the turbulence (particle wakes, mass loading, enhanced dissipation, see Balachandar and Eaton (2010)) may account for the observed discrepancies. The weaker tendency to cluster in the experiments is possibly an indication that the interactions between particles and turbulent structures are not well modeled, or that unaccounted physical effects (e.g. particle charge) play a significant role in the experiments.

We underline that the present study is among the very few to directly address quantitative differences in a one-to-one comparison between measurements and simulations at matching conditions. The results clearly show that further investigations are warranted to ultimately achieve reliable predictive models of particle-laden turbulent flows.

Acknowledgments

The authors acknowledge grants G00003613-ArmyW911NF-17-0366 from the U.S. Army Research Office and N00014-16-1-2472 from the Office of Naval Research. Computational resources were provided by the High Performance Computing Modernization Program (HPCMP), and by the ND Center for Research Computing.

References

Akiki, G., Moore, W., Balachandar, S., 2017. Pairwise-interaction extended point-particle model for particle-laden flows. J. Comput. Phys. 351, 329–357.
Baker, L., Frankel, A., Mani, A., Coletti, F., 2017. Coherent clusters of inertial particles in homogeneous turbulence. J. Fluid Mech. 833, 364–398.
Balachandar, S., Eaton, J.K., 2010. Turbulent dispersed multiphase flow. Annu. Rev. Fluid. Mech. 42, 111–133.
Barkley, D., Tuckerman, L.S., 2007. Mean flow of turbulent–laminar patterns in plane Couette flow. J. Fluid Mech. 576, 109–137.
Benson, M., Tanaka, T., Eaton, J.K., 2005. Effects of wall roughness on particle velocities in a turbulent channel flow. J. Fluids Eng. 127 (2), 250–256.
Bragg, A.D., Ireland, P.J., Collins, L.R., 2015. Mechanisms for the clustering of inertial particles in the inertial range of isotropic turbulence. Phys. Rev. E 92 (2), 023029.
Capecelatro, J., Desjardins, O., 2013. An Euler–Lagrange strategy for simulating particle-laden flows. J. Comput. Phys. 238, 1–31.
Capecelatro, J., Desjardins, O., 2015. Mass loading effects on turbulence modulation by particle clustering in dilute and moderately dilute channel flows. J. Fluids Eng. 137 (11), 111102.
Capecelatro, J., Desjardins, O., Fox, R.O., 2016. Strongly coupled fluid-particle flows in vertical channels. I. Reynolds-averaged two-phase turbulence statistics. Phys. Fluids 28 (3), 033306.
Capecelatro, J., Desjardins, O., Fox, R.O., 2018. On the transition between turbulence regimes in particle-laden channel flows. J. Fluid Mech. 845, 499–519.
Costa, P., Brandt, L., Picano, F., 2019. Interface-resolved simulations of small inertial particles in turbulent channel flow. arXiv:1906.01249.

Dritselis, C.D., Vlachos, N.S., 2008. Numerical study of educed coherent structures in the near-wall region of a particle-laden channel flow. Phys. Fluids 20 (5), 055103.
Eaton, J.K., 2009. Two-way coupled turbulence simulations of gas-particle flows using point-particle tracking. Int. J. Multiph. Flow 35 (9), 792–800.
Eaton, J.K., Fessler, J., 1994. Preferential concentration of particles by turbulence. Int. J. Multiph. Flow 20, 169–209.
Fessler, J.R., Kulick, J.D., Eaton, J.K., 1994. Preferential concentration of heavy particles in a turbulent channel flow. Phys. Fluids 6 (11), 3742–3749.
Fong, K.O., Amili, O., Coletti, F., 2019. Velocity and spatial distribution of inertial particles in a turbulent channel flow. J. Fluid Mech. 872, 367–406.
Gibilaro, L., Gallucci, K., Di Felice, R., Pagliai, P., 2007. On the apparent viscosity of a fluidized bed. Chem. Eng. Sci. 62 (1–2), 294–300.
Gualtieri, P., Picano, F., Casciola, C., 2009. Anisotropic clustering of inertial particles in homogeneous shear flow. J. Fluid Mech. 629, 25–39.
Gualtieri, P., Picano, F., Sardina, G., Casciola, C.M., 2013. Clustering and turbulence modulation in particle-laden shear flows. J. Fluid Mech. 715, 134–162.
Horwitz, J., Mani, A., 2016. Accurate calculation of stokes drag for point–particle tracking in two-way coupled flows. J. Comput. Phys. 318, 85–109.
Ireland, P.J., Desjardins, O., 2017. Improving particle drag predictions in euler–lagrange simulations with two-way coupling. J. Comput. Phys. 338, 405–430.
Kaftori, D., Hetsroni, G., Banerjee, S., 1995. Particle behavior in the turbulent boundary layer. i. motion, deposition, and entrainment. Phys. Fluids 7 (5), 1095–1106.
Kaftori, D., Hetsroni, G., Banerjee, S., 1995. Particle behavior in the turbulent boundary layer. ii. velocity and distribution profiles. Phys. Fluids 7 (5), 1107–1121.
Kim, J., Moin, P., Moser, R., 1987. Turbulence statistics in fully developed channel flow at low Reynolds number. J. Fluid Mech. 177, 133–166.
Klinkenberg, J., Sardina, G., De Lange, H., Brandt, L., 2013. Numerical study of laminar-turbulent transition in particle-laden channel flow. Phys. Rev. E 87 (4), 043011.
Klinkenberg, J., Sardina, G., De Lange, H., Brandt, L., 2011. Modal and non-modal stability of particle-laden channel flow. Phys. Fluids 23 (6), 064110.
Kloss, C., Goniva, C., Hager, A., Amberger, S., Pirker, S., 2012. Models, algorithms and validation for opensource DEM and CFD–DEM. Progr. Comput. Fluid Dyn. Int. J. 12 (2–3), 140–152.
Kuerten, J.G., Vreman, A., 2015. Effect of droplet interaction on droplet-laden turbulent channel flow. Phys. Fluids 27 (5), 053304.
Kulick, J.D., Fessler, J.R., Eaton, J.K., 1994. Particle response and turbulence modification in fully developed channel flow. J. Fluid Mech. 277, 109–134.
Lee, J., Lee, C., 2015. Modification of particle-laden near-wall turbulence: effect of stokes number. Phys. Fluids 27 (2), 023303.
Li, Y., McLaughlin, J.B., Kontomaris, K., Portela, L., 2001. Numerical simulation of particle-laden turbulent channel flow. Phys. Fluids 13 (10), 2957–2967.
Marchioli, C., Picciotto, M., Soldati, A., 2007. Influence of gravity and lift on particle velocity statistics and transfer rates in turbulent vertical channel flow. Int. J. Multiph. Flow 33 (3), 227–251.
Marchioli, C., Soldati, A., 2002. Mechanisms for particle transfer and segregation in a turbulent boundary layer. J. Fluid Mech. 468, 283–315.
Marchioli, C., Soldati, A., Kuerten, J., Arcen, B., Taniere, A., Goldensoph, G., Squires, K., Cargnelutti, M., Portela, L., 2008. Statistics of particle dispersion in direct numerical simulations of wall-bounded turbulence: results of an international collaborative benchmark test. Int. J. Multiph. Flow 34 (9), 879–893.
Maxey, M., 2017. Simulation methods for particulate flows and concentrated suspensions. Annu. Rev. Fluid. Mech. 49, 171–193.
Maxey, M.R., Riley, J.J., 1983. Equation of motion for a small rigid sphere in a nonuniform flow. Phys. Fluids 26 (4), 883–889.
Monchaux, R., Bourgoin, M., Cartellier, A., 2012. Analyzing preferential concentration and clustering of inertial particles in turbulence. Int. J. Multiph. Flow 40, 1–18.
de Motta, J.B., Costa, P., Derksen, J., Peng, C., Wang, L.-P., Breugem, W.-P., Estivalezes, J., Vincent, S., Climent, E., Fede, P., et al., 2019. Assessment of numerical methods for fully resolved simulations of particle-laden turbulent flows. Comput. Fluids 179, 1–14.
Narayanan, C., Lakehal, D., Botto, L., Soldati, A., 2003. Mechanisms of particle deposition in a fully developed turbulent open channel flow. Phys. Fluids 15 (3), 763–775.
Nasr, H., Ahmadi, G., McLaughlin, J.B., 2009. A DNS study of effects of particle–particle collisions and two-way coupling on particle deposition and phasic fluctuations. J. Fluid Mech. 640, 507–536.
Nilsen, C., Andersson, H.I., Zhao, L., 2013. A Voronoï analysis of preferential concentration in a vertical channel flow. Phys. Fluids 25 (11), 115108.
Pan, Y., Banerjee, S., 1995. A numerical study of free-surface turbulence in channel flow. Phys. Fluids (1994-present) 7 (7), 1649–1664.
Pan, Y., Banerjee, S., 1996. Numerical simulation of particle interactions with wall turbulence. Phys. Fluids 8 (10), 2733–2755.
Paris, A.D., 2001. Turbulence attenuation in a particle-laden channel flow. PhD dissertation at Stanford University in 2011.
Petersen, A.J., Baker, L., Coletti, F., 2019. Experimental study of inertial particles clustering and settling in homogeneous turbulence. J. Fluid Mech. 864, 925–970.
Poelma, C., Ooms, G., 2006. Particle-turbulence interaction in a homogeneous, isotropic turbulent suspension. Appl. Mech. Rev. 59 (2), 78–90.
Richter, D.H., Sullivan, P.P., 2013. Momentum transfer in a turbulent, particle-laden Couette flow. Phys. Fluids (1994-present) 25 (5), 053304.
Richter, D.H., Sullivan, P.P., 2014. Modification of near-wall coherent structures by inertial particles. Physics of Fluids (1994-present) 26 (10), 103304.
Rouson, D.W., Eaton, J.K., 2001. On the preferential concentration of solid particles in turbulent channel flow. J. Fluid Mech. 428, 149–169.
Sardina, G., Schlatter, P., Brandt, L., Picano, F., Casciola, C.M., 2012. Wall accumulation and spatial localization in particle-laden wall flows. J. Fluid Mech. 699, 50–78.
Schiller, V., 1933. Ber die grundlegenden berechnungen bei der schwerkraftaufbereitung. Z. Vereines Deutscher Inge. 77, 318–321.
Squires, K., 2007. Point-particle methods for disperse flows. In: Computational Methods for Multiphase Flow. Cambridge University Press, pp. 282–319.
Sumer, B.M., Deigaard, R., 1981. Particle motions near the bottom in turbulent flow in an open channel. Part 2. J. Fluid Mech. 109, 311–337.
Sundaram, S., Collins, L.R., 1997. Collision statistics in an isotropic particle-laden turbulent suspension. Part 1. Direct numerical simulations. J. Fluid Mech. 335, 75–109.
Vreman, A., 2015. Turbulence attenuation in particle-laden flow in smooth and rough channels. J. Fluid Mech. 773, 103–136.
Vreman, B., Geurts, B.J., Deen, N., Kuipers, J., Kuerten, J.G., 2009. Two-and four-way coupled Euler–Lagrangian large-eddy simulation of turbulent particle-laden channel flow. Flow Turbul. Combust. 82 (1), 47–71.
Wang, G., Richter, D., 2019a. Modulation of the turbulence regeneration cycle by inertial particles in planar Couette flow. J. Fluid Mech. 861, 901–929.
Wang, G., Richter, D., 2019b. Transport and two-way coupling effect of inertial particles by large-scale and very-large-scale motions in turbulence. arXiv:1906.01779.
Wang, G., Richter, D.H., 2019c. Two mechanisms of modulation of very-large-scale motions by inertial particles in open channel flow. J. Fluid Mech. 868, 538–559. doi:10.1017/jfm.2019.210.
Wang, L.-P., Maxey, M.R., 1993. Settling velocity and concentration distribution of heavy particles in homogeneous isotropic turbulence. J. Fluid Mech. 256, 27–68.
Zhao, L., Andersson, H.I., Gillissen, J.J., 2013. Interphasial energy transfer and particle dissipation in particle-laden wall turbulence. J. Fluid Mech. 715, 32.